UNIVERSITY
OF MICHIGAN

MAR 21 1955

ENGINEERING
LIBRARY

THE AERONAUTICAL QUARTERLY

Volume III SEPTEMBER 1951 Part II

CONTENTS

The Construction and Testing of a Xylonite Model of a Delta Aircraft — *S. C. Redshaw and P. J. Palmer*

A Note on the Stressing of Oleo-Pneumatic Shock Absorbers — *D. M. A. Leggett*

The Flow of an Incompressible Fluid through an Axial Turbo-Machine with any Number of Rows — *J. W. Railly*

The Anti-Symmetric Vibrations of Aircraft — *R. W. Traill-Nash*

LONDON
ROYAL AERONAUTICAL SOCIETY
4 HAMILTON PLACE W1

10/-

THE AERONAUTICAL QUARTERLY

Editorial Board

Dr. H. ROXBEE COX, D.I.C., F.R.Ae.S., F.I.Ae.S.

Professor S. GOLDSTEIN, F.R.S., F.R.Ae.S.

Sir GEOFFREY TAYLOR, F.R.S.

G. H. DOWTY, F.R.Ae.S. (Chairman of the JOURNAL Committee of the Royal Aeronautical Society)

J. SMITH, C.B.E., F.R.Ae.S., A.M.I.Mech.E. (Chairman of the Technical Board and Executive Committee of the Society of British Aircraft Constructors)

Joint Editors

Dr. A. M. Ballantyne, T.D., A.F.R.Ae.S.
Joan Bradbrooke, A.R.Ae.S.

Editorial Referees

Aerodynamics

(a) General

Prof. L. BAIRSTOW
Dr. G. P. DOUGLAS
Prof. A. A. HALL
Sir B. MELVILL JONES
Mr. D. KEITH-LUCAS
Dr. N. A. V. PIERCY
Mr. E. F. RELF
Prof. E. J. RICHARDS

(b) Fluid Motion

Mr. A. FAGE
Prof. S. GOLDSTEIN
Prof. L. HOWARTH
Mr. W. P. JONES
Prof. M. J. LIGHTHILL
Dr. J. W. MACCOLL
Dr. J. H. PRESTON
Mr. L. F. G. SIMMONS
Mr. H. B. SQUIRE
Sir GEOFFREY TAYLOR
Prof. G. TEMPLE
Prof. A. D. YOUNG

(c) Stability and Control

Mr. L. W. BRYANT
Mr. S. B. GATES
Mr. G. T. R. HILL
Mr. H. B. IRVING
Mr. G. H. LEE
Mr. M. B. MORGAN

Helicopters and Propellers

Dr. J. A. J. BENNETT
Mr. L. G. FAIRHURST
Mr. R. HAFNER
Capt. R. N. LIPTROT
Mr. J. MULLIN

Instruments and Electrical Equipment

Dr. G. E. BAIRSTO
Mr. G. W. H. GARDNER
Mr. C. S. HUDSON
Mr. A. N. IRENS
Mr. C. N. JAQUES
Mr. F. W. MEREDITH

Aircraft Design

Mr. R. BOORMAN
Mr. R. M. CLARKSON
Mr. A. N. CLIFTON
Mr. W. S. FARREN
Mr. H. H. GARDNER
Mr. H. KNOWLER
Mr. W. E. W. PETTER
Mr. F. H. POLLICUTT
Mr. A. E. RUSSELL
Mr. R. S. STAFFORD

Radio and Radar

Mr. J. F. ATHERTON
Mr. B. G. GATES
Mr. R. L. SMITH ROSE
Dr. A. M. UTTLEY
Sir ROBERT WATSON WATT

Aviation Medicine

Dr. A. BUCHANAN BARBOUR

Meteorology

Prof. D. BRUNT
Mr. J. K. HARDY
Prof. P. A. SHEPPARD

Sound

Mr. N. FLEMING
Mr. W. MAKINSON

Aircraft Propulsion

Mr. H. CONSTANT
Sir A. H. ROY FEDDEN
Dr. S. HOOKER
Mr. A. R. HOWELL
Mr. P. LLOYD
Dr. A. W. MORLEY
Dr. E. S. MOULT
Mr. N. S. MUIR
Mr. F. NIXON
Mr. F. M. OWNER
Dr. D. PYE
Mr. H. SAMMONS
Prof. O. A. SAUNDERS

Air Transport

Mr. P. G. MASEFIELD
Mr. N. E. ROWE
Mr. W. TYE

Aircraft Accessories

Mr. W. C. CLOTHIER
Mr. H. G. CONWAY
Mr. G. H. DOWTY
Mr. R. GRAHAM

Vibration and Flutter

Prof. A. R. COLLAR
Prof. W. J. DUNCAN
Mr. R. A. FRAZER
Dr. A. ROBINSON
Mr. H. TEMPLETON

Performance

Mr. H. DAVIES
Mr. D. R. NEWMAN
Mr. A. H. YATES

Structures

Mr. A. C. BROWN
Mr. H. L. COX
Mr. D. J. FARRAR
Dr. H. ROXBEE COX
Prof. W. S. HEMP
Mr. H. B. HOWARD
Mr. E. D. KEEN
Mr. F. A. KERRY
Dr. D. M. A. LEGGETT
Prof. R. L. LICKLEY
Prof. A. J. SUTTON PIPPARD
Prof. A. G. PUGSLEY
Prof. S. C. REDSHAW
Mr. R. H. SANDIFER
Sir RICHARD SOUTHWELL

Fuels and Oils

Mr. E. L. BASS
Mr. J. W. DRINKWATER
Prof. F. H. GARNER
Prof. W. E. GARNER
Dr. K. E. W. RIDLER
Dr. C. G. WILLIAMS

Materials

Prof. L. AITCHISON
Dr. N. P. ALLEN
Prof. N. F. MOTT
Mr. L. ROTHERHAM
Dr. H. SUTTON
Dr. C. SYKES

Flight Testing

Mr. P. A. HUFTON
Mr. E. T. JONES
Mr. S. SCOTT HALL
Mr. H. L. STEVENS

The Construction and Testing of a Xylonite Model of a Delta Aircraft

S. C. REDSHAW†, M.Sc., Ph.D., M.I.C.E., F.R.Ae.S.
(Professor of Civil Engineering, University of Birmingham)

and

P. J. PALMER, B.Sc., A.R.C.S., D.I.C., Grad.R.Ae.S.
(Technical Office, Boulton Paul Aircraft Limited)

Summary: In order to provide information to assist with the unorthodox design of a delta aircraft, an accurate scale model in Xylonite was designed and constructed.

The reasons for the selection of the particular scale factors so that the model could be used for stiffness, strain distribution, resonance and flutter tests are discussed.

A description is given of the special test instruments which were developed, together with an account of the control tests and the tests to which the model was subjected.

Finally, a comparison is made with the actual tests which were made on the full-scale aircraft at a later date. The full-scale and model results were found to be in good agreement.

1. Introduction

With the advent of stressed skin structures in aircraft construction the difficulties of the stress analyst were considerably increased. Whereas with the earlier type of braced frame structure, statically determinate or redundant, a reasonably precise analysis could be made, with stressed skin construction problems of indeterminancy were considerably complicated. The vast volume of theoretical and experimental research in recent years has enabled a structural analysis of an all-metal aircraft structure, having wings of little or no sweep and moderate or high aspect ratio, to be made with fair accuracy.

Recent developments in aerodynamic wing design have called for wings with high sweep and taper ratio and low aspect ratio; such structures are extremely

†Formerly Chief Engineer, Boulton Paul Aircraft Limited.

Paper received April 1951.
[The Aeronautical Quarterly, Vol. III, September 1951]

difficult to analyse theoretically, and a full-scale test for the purpose of providing design information would be costly and could not be made in time to provide useful information for the particular design in question.

In addition, with high-speed aircraft, it is necessary to predict the flutter speeds with reasonable accuracy. Before a flutter analysis can be made it is necessary to have data regarding the stiffness of the wing and its resonant modes of vibration; for unconventional wing forms the obtaining of this information presents similar theoretical difficulties to the determination of the stress distribution.

During the early stages in the design of a delta aircraft it was realised that it would be necessary to supplement theoretical calculations by an experimental analysis, in order to solve some of the new structural design problems which arose.

Considerable experience had been obtained in the design and construction of Xylonite structural models, some six models having been built by Boulton Paul Aircraft Ltd. since 1942; the tests on one of the earliest of these models has been reported previously[1]. It was a natural step that, with encouragement from the Ministry of Supply, a model should be built for the purpose of investigating wing stiffness, strain distribution, ground resonance and wind-tunnel flutter characteristics. It must be emphasised that time was an important factor in this scheme of research; the greater part of the model had to be an exact representation of the full-scale aircraft and therefore had to be made from the same drawings, and yet it had to be built and tested before the full-scale aircraft was completed so that information from the model tests would be available before the first flight of the prototype. At the same time it was essential that the prototype design and construction should not be delayed because of the model work.

Notation

Suffixes " F " and " M " refer to full scale and to model.
Physical dimensions of the quantities are given in parentheses.

E	modulus of elasticity ($ML^{-1}T^{-2}$)
E_D	dynamic modulus of elasticity ($ML^{-1}T^{-2}$)
k	a coefficient, factor by which the true scale thickness of model material is increased
l	typical length (L)
P	applied load (MLT^{-2})
r	(gravity angular deflection for model)/(gravity angular deflection for full scale)
t	thickness (L)
V	speed (LT^{-1})
V_c	critical flutter speed (LT^{-1})
v	velocity of wave propagation (LT^{-1})

w loading from weight distribution (MT^{-2})

W weight (MLT^{-2})

γ material density (ML^{-3})

λ (full scale length)/(model length)

μ damping factor (T^{-1})

ν kinematic viscosity of air (L^2T^{-1})

ρ air density (ML^{-3})

σ Poisson's ratio

ω resonance frequency (T^{-1})

2. The Design of the Model

2.1. The selection of the material for the model

On account of aeolotropy, wood is not a suitable material for a structural model, and the choice therefore remained between metal and a plastic material. If a model had been required solely for stiffness and strain distribution tests, a metal model could have been considered, although the fabrication of such a model, particularly the jointing of components, would have been difficult. For flutter tests, in order to avoid high tunnel speeds, a material of reduced modulus of elasticity-density ratio is required and therefore it was necessary to use a suitable plastic material. Xylonite had been used successfully on previous occasions and therefore it was selected again for the present purpose.

2.2. Description of Xylonite

Alexander Parkes, a Birmingham technologist, while studying nitrocellulose discovered that by adding camphor to collodion solutions he could overcome what he called the "contractile tendency of nitrocellulose." His invention was developed in the United States in the form of celluloid, while in this country The British Xylonite Company was formed and produced a material under the trade name of "Xylonite." This material is thermoplastic and can be produced in either coloured or transparent form. One of its most impressive features is the great ease with which it can be manipulated. Owing to its thermoplastic nature Xylonite can be pressed when hot into various shapes and the heating and cooling cycle may be repeated any number of times. It can be stretched, sawn, turned, cut, bent, moulded and punched with great ease and accuracy, and its moulding qualities are excellent. In model work a most important feature is the ease whereby pieces of the material can be cemented together with a solution of 40 per cent. amyl acetate and 60 per cent. acetone to give a strong and reliable joint. The material can be supplied in sheet, rod and tube form. The ease of fabrication and jointing, in addition to the variety of forms in which it can be supplied, give Xylonite a

superiority over Perspex (methyl methacrylate) for model work. Cellulose acetate materials are inferior to materials with a cellulose nitrate base because of dimensional instability.

2.3. *Physical properties of Xylonite*

Clear transparent Xylonite, Formula 16495, was used for the model. The physical properties of the material from which a flexible model is to be built, are of considerable importance and great care was exercised in determining them.

It is necessary to know the specific gravity, the modulus of elasticity, either the modulus of rigidity or Poisson's ratio, the tensile strength, strain-creep characteristics and the effect of temperature and humidity on the elastic constants. In addition, Xylonite, like most plastics, possesses both static and dynamic values of the elastic constants and both must be determined.

It was realised that fundamental research on the effect of wide variations of temperature and humidity on the elastic constants would be beyond the scope of the investigation and it was decided therefore to make all the tests in the same laboratory, maintaining a condition of constant temperature and humidity. Unfortunately, although it was possible to keep the temperature sensibly constant, a slight change in humidity was unavoidable without recourse to a special humidity-controlled chamber.

All the material control tests were made in the one laboratory side by side with the model tests, the controls being checked each time a model test was made, thus ensuring that the temperature and humidity conditions were the same for both controls and model.

2.3.1. *Specific gravity*

The density of a few samples of Xylonite sheeting was determined by weighing and measuring the volumes, and a density of 0.049 lb./in.^{3} was obtained. This corresponds to a specific gravity of 1.36.

2.3.2. *Modulus of elasticity*

It was necessary to measure both the static and dynamic values of the modulus of elasticity. In both cases, the specimens used were cut from the actual sheets used in the construction of the model, and each specimen was marked with an indication of the location of the particular sheet from which it was taken on the model.

For the static modulus of elasticity, the method of test can be seen from Fig. 1. The specimen was suspended vertically, the load being applied by weights. Two micrometer eye-piece microscopes were used to observe the relative movement of two lines drawn at a prescribed distance apart on the specimen. The mean value for the static modulus of elasticity of the specimens measured was found

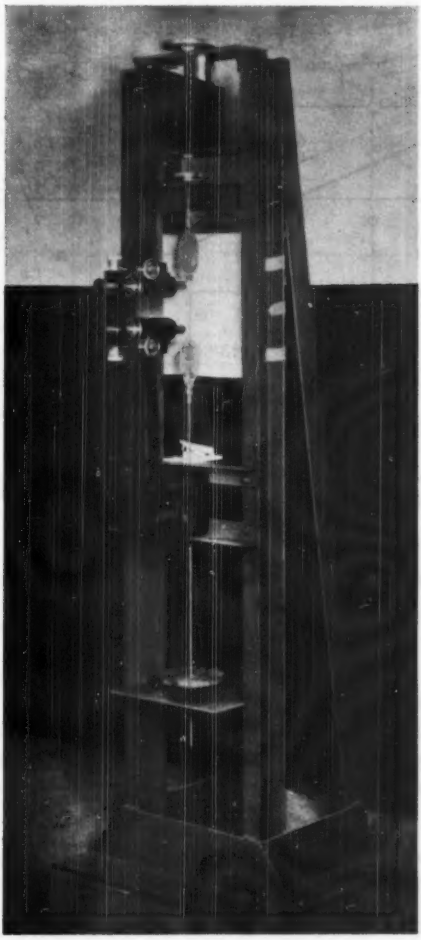

Fig. 1.
Apparatus for the measurement of the modulus of elasticity of Xylonite specimens.

to be 0.35×10^6 lb./in.^{2} at 65°F. No accurate variation of this value with sheet thickness, relative humidity and temperature was obtained, but it can be said that the trends are for the static modulus of elasticity to decrease with all these three parameters.

Figure 2 shows the results obtained by measuring the static modulus of elasticity of a single 0.025 in. specimen for several values of relative humidity, the temperature

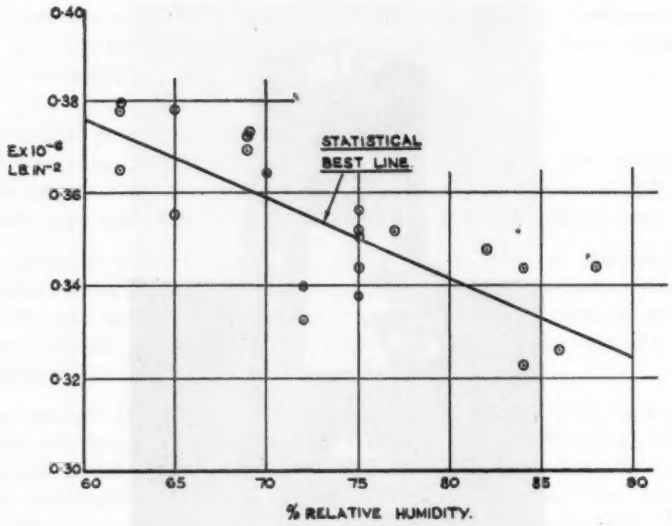

Fig. 2.
Variation of modulus of elasticity with relative humidity.
Single tensile specimen of 0.025 in. Xylonite.
Temperature constant at 65°F.

being kept constant at 65°F. One reason for the large amount of scatter, no doubt, is the fact that the specimen should have been kept at a particular relative humidity value for several hours before its modulus was measured. This was not possible with the equipment available and so the actual relative humidity value, recorded at the time of test, may not be truly representative of the condition of the specimen.

The limit of proportionality for Xylonite sheets as tested was about 3,500 lb./in.², and the ultimate strength was 8,000 to 8,500 lb./in.²

A report by Baker[2] gives a static modulus of elasticity for cellulose nitrate of 0.4×10^6 lb./in.² at 20°C. and 30 per cent. relative humidity falling to 0.28×10^6 lb./in.² at 20°C. and 100 per cent. relative humidity. This same report gives an ultimate strength for cellulose nitrate of 10,200 lb./in.² at 20°C. and 30 per cent. relative humidity, falling to 6,400 lb./in.² at 20°C. and 100 per cent. relative humidity.

Further work on the variation of the mechanical properties of cellulose nitrate with temperature and humidity is contained in a report by Lawton, Carswell and Nason[3].

A pair of typical creep curves for Xylonite when subjected to a tensile load are shown in Fig. 3. It will be seen that very little creep occurs after two minutes, so

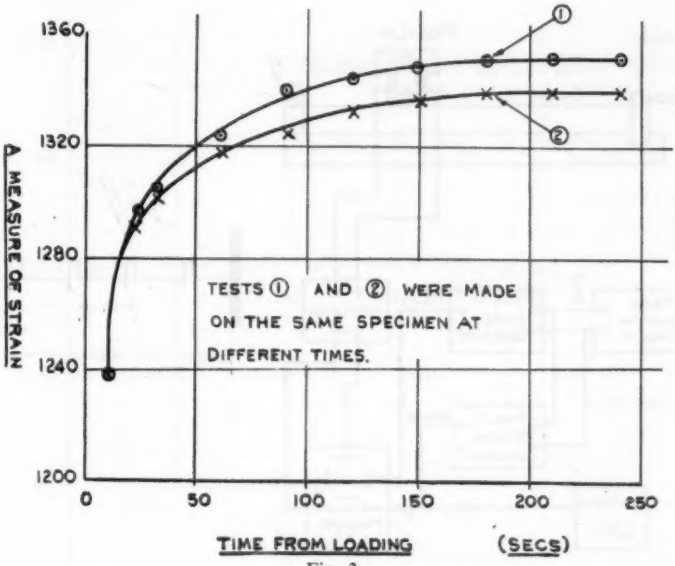

Fig. 3.
Typical creep curves for Xylonite.
Measurements were made by means of electric strain gauges
mounted on a specimen subjected to a tensile load.
Specimen: 0.75 in. x .030 in.
Load: 6 lb.
Stress: 267 lb./sq in.

in all tests, both control and model, measurements with static loads were made two minutes after the application of the load.

A similar curve is obtained in a report by Bruhn[4] and this report also shows that the static modulus of elasticity for nitrocellulose decreases with increasing sheet thickness.

If the temperature was kept constant at 65°F., then over the range of humidities encountered and for the sheet thicknesses used, it is quite satisfactory to consider the static modulus of elasticity for Xylonite as being 0.35×10^6 lb./in.^{2}

The dynamic modulus of elasticity was measured by the method of Pinoir and Dubois[5] which consists of measuring the velocity of propagation of longitudinal waves in the material under test. A diagram of the circuit used in the present investigation is shown in Fig. 4. A long strip of Xylonite is subjected to a tensile loading and one end is then given an impulse by an electrical vibrator. This impulse is then detected further along the strip by means of an electrical pick-up and the time of transmission of the wave is measured by recording on a cathode ray oscilloscope. The value for the dynamic modulus of elasticity is then given by

$$E_D = v^2 \gamma .$$

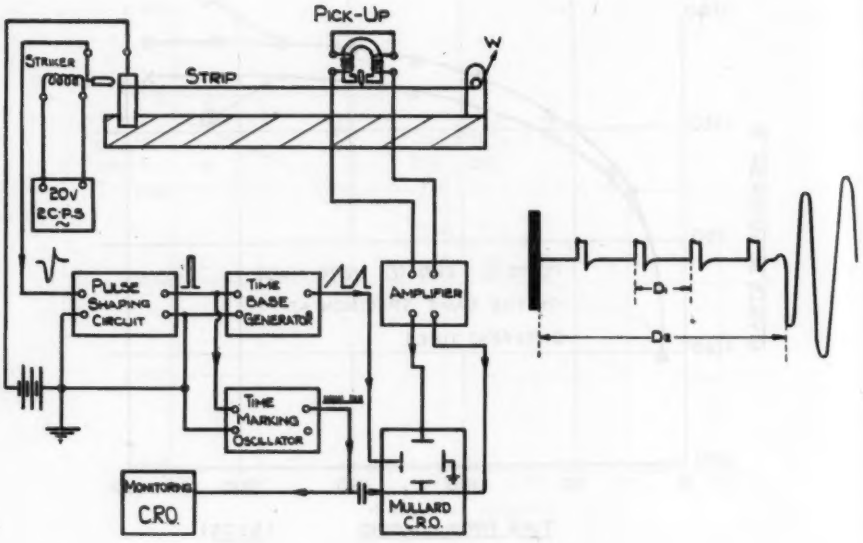

Fig. 4.

Schematic diagram of apparatus for measurement of sound velocity.

$D_1 \propto$ period of timing marker
$D_2 \propto$ transit time of sound wave
Form of presentation on cathode ray tube.

The mean value determined after tests on several Xylonite specimens was 0.51×10^6 lb./in.^{2} at 65°F.

2.3.3. *Poisson's ratio*

It would be difficult to measure the value of Poisson's ratio for thin Xylonite sheets by the normal extensometer method, because the weight of the extensometer would become an appreciable factor.

Two other methods were tried. Firstly, by bending a Xylonite blade and measuring the two curvatures. The longitudinal curvature was obtained by measuring the deflection of the centre of the beam by a vernier microscope, and the lateral curvature was measured by means of a pair of fine, light needles mounted on the edges of the blade and normal to its plane. The second method used was the optical interference method of Cornu[6].

Neither of these methods was entirely satisfactory because of the small thickness of the specimens used. In the Cornu method, it was found to be difficult to get a specimen with an optically flat surface, and without any initial curvature.

The value for Poisson's ratio obtained by these methods was approximately 0.39.

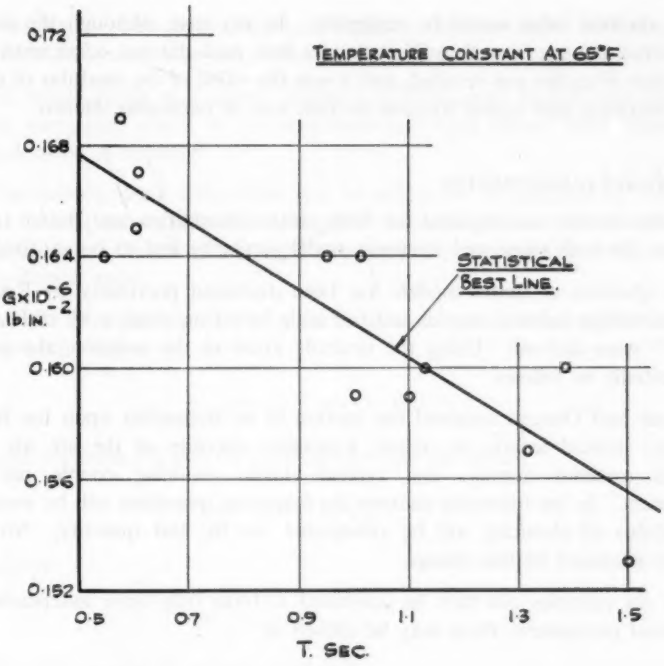

Fig. 5.
Modulus of rigidity by torsional oscillations of a blade.

2.3.4. *Modulus of rigidity*

No satisfactory method was available for the measurment of either the absolute static or dynamic value of the modulus of rigidity, but the method of Searle[7], by the torsion of a blade, should give values of the modulus of rigidity which are dependent upon the period of oscillation. A few values for the modulus of rigidity were obtained by this method, and are presented in Fig. 5. In spite of the scatter due to changes in humidity and the different specimens being used, it can be seen that the trend is for the modulus value to decrease as the period of oscillation increases.

It should be pointed out that if the value of the modulus of rigidity corresponding to two cycles per second is taken, say 0.168×10^6 lb./in.^{2}, then the corresponding modulus of elasticity would be $0.168 \times 10^6 \times 2 \times 1.39 = 0.47 \times 10^6$ lb./in.^{2}, assuming Poisson's ratio to be the same under both static and dynamic conditions. This value for the modulus of elasticity is more than the static value and slightly less than the absolute dynamic value, but it is fair to assume that by the time a frequency of eight cycles per second is reached (corresponding to the lower end of the resonance tests frequency range), the difference between this value

and the absolute value would be negligible. In any case, although the resonance tests covered a range from 8 to 75 cycles the first peak did not occur until a value greater than 30 cycles was reached, and it was the value of the modulus of elasticity at this frequency and higher frequencies that was of particular interest.

2.4. *Model relationships*

As the model was required for both strain distribution and flutter tests, the conditions for both static and dynamic model similarity had to be satisfied.

The question of flutter models has been discussed previously by Redshaw[8] and relationships between model and full scale based on some work of Frazer and Duncan[9] were derived. Using the symbols given in the notation, the argument was essentially as follows.

Frazer and Duncan assumed the motion to be dependent upon the following quantities: typical length, air speed, kinematic viscosity of the air, air density, structural material density, and typical elastic restoring couple per radian displacement. In the following analysis the foregoing quantities will be used except that modulus of elasticity will be substituted for the last quantity. No loss in generality is caused by this change.

The six variables can then be combined to form only three independent non-dimensional parameters; these may be chosen as

$$\rho/\gamma, Vl/\nu \text{ and } \rho V^2/E.$$

The argument of Frazer and Duncan may be applied to the present case, the only difference being in the use of $\rho V^2/E$ as the third parameter.

Following Frazer and Duncan, the damping factor μ must be expressible in the functional form

$$\mu=(V/l)\, F(\rho/\gamma, Vl/\nu, \rho V^2/E) \quad . \quad . \quad . \quad . \quad (1)$$

For the equality of the three parameters the following relations must be satisfied:—

$$\rho_F/\gamma_F=\rho_M/\gamma_M \quad . \quad . \quad . \quad . \quad . \quad (2)$$

$$V_F l_F/\nu_F=V_M l_M/\nu_M \quad . \quad . \quad . \quad . \quad (3)$$

$$\rho_F V_F^2/E_F=\rho_M V_M^2/E_M \quad . \quad . \quad . \quad . \quad (4)$$

If the values of ρ and ν are the same for full scale and model, the densities of the material for full scale and model would also have to be equal.

If the length ratio of the full-scale aeroplane to the model has been decided upon, the E_F/E_M ratio can be found which would satisfy equations (3) and (4).

This would result in a model having a critical speed higher than that of the full-scale aeroplane, which would be useless for wind tunnel experiments where a reduced speed is required.

If the aerodynamic scale effect can be neglected, as assumed by Frazer and Duncan, then equation (3) may be discarded and the critical speed for the model can be made lower than that for the full-scale aircraft by using a material of reduced elasticity-density ratio.

The ratio of critical speed V_c for full scale and model, deduced from equations (2) and (4) will be

$$V_{cF}/V_{cM} = \{ (E/\gamma)_F/(E/\gamma)_M \}^{\frac{1}{2}} \quad . \quad . \quad . \quad (5)$$

Again, equation (2) may be transformed into the form

$$w_F/w_M = \lambda^2 \rho_F/\rho_M \quad . \quad . \quad . \quad . \quad . \quad . \quad (6)$$

and similarly

$$W_F/W_M = \lambda^3 \rho_F/\rho_M \quad . \quad . \quad . \quad . \quad . \quad (7)$$

where W is the weight of an individual unit.

Now if λ and the densities of the materials have been decided upon, equations (6) and (7) must, in general, be inconsistent if $\rho_F = \rho_M$. To overcome this difficulty a variable-density wind tunnel could be used to give a reduced air density in which case an exact solution to the problem would be obtained. Unfortunately, in practically all cases, this would result in a low value for Reynolds number.

Fortunately, a different approach to the problem is possible. With the modern stressed-skin type of aeroplane construction the thickness of the material is small compared with other dimensions and the stress distribution across the skin thickness, or the transverse section of a member, may be considered to be constant.

For dynamic similarity, the mass and stiffness of the model must be distributed identically with those of the full-scale aeroplane.

Now suppose a model were constructed true to scale with regard to external dimensions but having the thickness of the material increased from t to kt, where k is some coefficient.

Since the material thickness is everywhere assumed to be small compared with all the other linear dimensions, the inertia and stiffness distributions of the model of which the thickness has been increased in the ratio k, are identical to a model

possessing perfect geometric similarity but having the modulus of elasticity and the density of its material increased from E and γ to kE and $k\gamma$ respectively. As the external dimensions are the same, the two models are aerodynamically similar and the flutter characteristics will be identical.

If kE_M, and $k\gamma_M$ are substituted for E_M and γ_M in equations (2) and (4) the following relationships are obtained for a model in which the material thickness has been multiplied by k.

$$\rho_F/\gamma_F=\rho_M/(k\gamma_M) \quad . \quad . \quad . \quad . \quad . \quad (8)$$

$$\rho_F V_F^2/E_F=\rho_M V_M^2/(kE_M) \quad . \quad . \quad . \quad . \quad (9)$$

Equation (5) may then be obtained from these equations, and equation (6) may be expressed in the form

$$\lambda^2 \rho_F/\rho_M=(\gamma lt)_F/(\gamma lt)_M \quad . \quad . \quad . \quad . \quad (10)$$

where l is the length of a section, and t is its thickness.

The foregoing method presents a most advantageous solution to the problem as the use of thicker material is of considerable practical help in the construction of the model.

Scruton and Lambourne[10] have stated that it may not always be possible to ignore the gravitational parameter $\rho gl/E$, remarking that the effect of gravity on the trim of a flexible model wing mounted horizontally may be considerable if the gravitational parameters for model and full scale are widely different. Thus the speed and linear scales cannot be fixed independently but should be connected by a relation

$$r=(1/\lambda)(V_F/V_M)^2.$$

For a Xylonite model $V_F/V_M=3.06$ approximately, and therefore $r=9.3/\lambda$ approximately.

Scruton and Lambourne suggested that for most models the highest permissible value of r will be about 3.0. For the present model $\lambda=5.378$, and therefore $r=1.73$, which was considered to be satisfactory.

Table I gives a summary of the relationships between full scale and model and was constructed by using the values of the physical constants determined from the control tests. The dynamic value of the modulus of elasticity, E_D, for Xylonite was used in the calculation of the resonance frequency and flutter speed relationships.

The physical constants assumed for the full-scale aircraft are

$$E = 10 \times 10^6 \text{ lb./in.}^2$$

$$\gamma = 0.103 \text{ lb./in.}^3$$

$$\sigma = 0.30.$$

It is assumed that the ratio of the modulus of rigidity for the full-scale aircraft to the modulus of rigidity for the model, is the same as the ratio of the moduli of elasticity. This means that in the extreme case of pure shear, there is an implied error of

$$\left(\frac{1+\sigma_M}{1+\sigma_F} - 1\right) \times 100 \text{ per cent.} = 7 \text{ per cent.}$$

The rather peculiar scale factor of 5.378 was chosen partly because it was a factor that gave suitable Xylonite skin thicknesses, and partly because a solid model of this same scale was in existence and it was thought that comparative tunnel tests could ultimately be made.

The routine design procedure adopted was to use prints from the actual drawings which were issued for the full-scale aircraft, but with the linear dimensions altered in accordance with the values given in Table I.

TABLE I

Parameter	*Dependence of parameter*	*Multiplying factors to convert model value to full scale value*
Length	l	$5.378 = 1/0.186$
Thickness	t	$2.56 = 1/0.391$
Load per unit deflection	Et	$73.1 = 1/0.0137$
Torque per unit twist	$l^2 Et$	$2115 = 1/0.000474$
Load for equal strains	$l\,tE$	$394 = 1/0.00254$
Buckling strain (flat panels)	$(t/l)^2$	$0.227 = 1/4.4$
Buckling strain (curved panels)	t/l	$0.476 = 1/2.1$
Resonance frequency	$(Et/l^3)^{\frac{1}{2}}$	$0.569 = 1/1.76$
Flutter speed	$(E/\gamma)^{\frac{1}{2}}$	$3.06 = 1/0.327$
Weight	l^3	$155.55 = 1/0.00643$

The wings, spar frames and other major components of the body were identical to the full-scale machine, but there were minor differences in other parts of the body. The nose and tail portions of the body were fairings of correct weight distribution. The parts of the body that differed from the full-scale aircraft were built not only with the correct weight, but also with the correct stiffness and, because of this, a simpler type of construction than used on the full-scale machine was possible. The parts constructed in this form made only minor contributions to the stiffness of the body, so that errors in stiffness of these altered components would have little effect on the stiffness of the body as a whole.

3. The Construction of the Model

3.1. General description of the structure

A general arrangement of the prototype aircraft structure is shown in Fig. 6. It will be seen that the torsion box formed by the leading edge and the front spar passes uninterrupted through the fuselage, the middle and rear spars being attached at the side of the fuselage to rings which are necessary for the installation of the engine.

It was decided that the model wing structure should be as completely representative of the full-scale wing as possible, no idealisation of the structure for the simplification of construction being acceptable. The undercarriage fuel tanks and items of equipment and instrumentation, which were housed within the wing, were all reproduced on the model. These items, although not constructed of Xylonite, were true to the correct scale factors.

The fuselage structure was representative of the full-scale aircraft as far as the centre portion only. No attempt was made to reproduce the front and rear portions of the fuselage and the fin and rudder, although front and rear fairings were provided for the wind-tunnel test and masses were located within the fuselage structure to preserve the correct model relationships. The mounting for the resonance and flutter tests was located in the engine bay, the mechanical oscillator being situated in the forward portion of the rear fuselage.

3.2. Fabrication of components

The components were made from the actual full-scale drawings, the dimensions being altered to the model values on the prints before issue. Details were marked out in the normal way and cut out ready for pressing into the correct shape. Light alloy tools were made for forming the components. These tools were heated in a water bath to a temperature of 100°C. A Xylonite component, which was at room temperature, was immediately placed in the tool and formed to shape under pressure. The tool was allowed to cool, the component being removed from it when cool, and immediately immersed in water at room temperature. The stringers were folded with one simple tool, but some of the heavier built-up type of ribs required several tools.

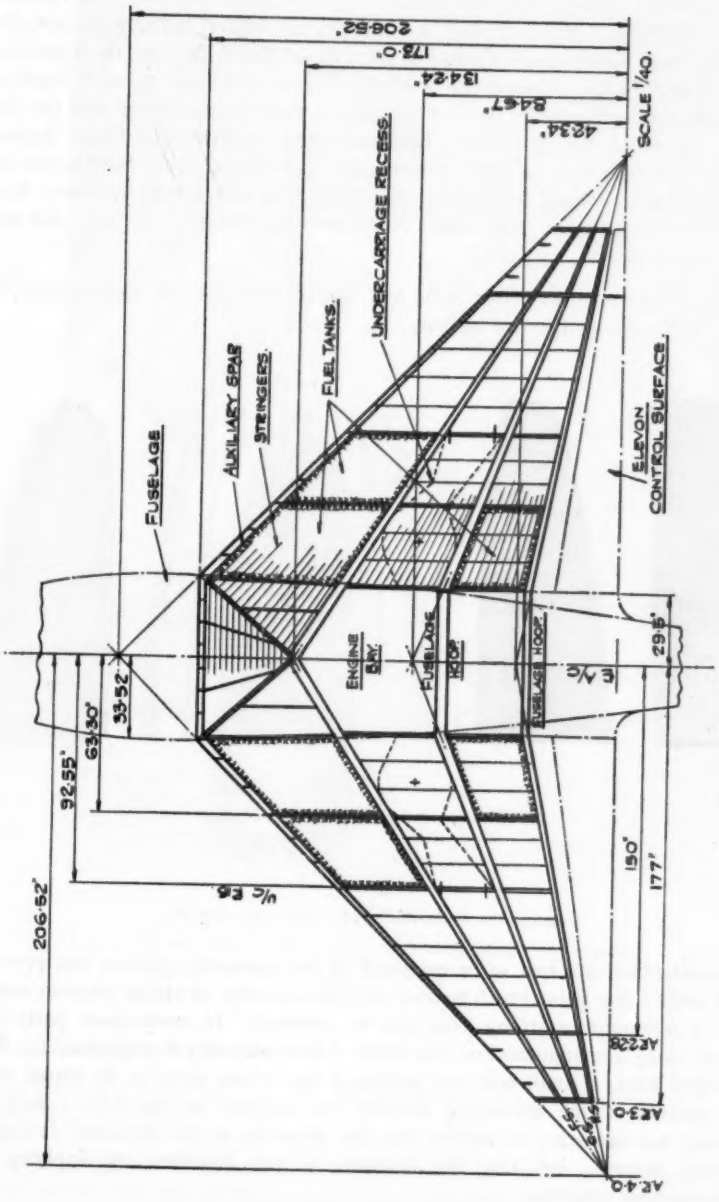

Fig. 6.
General arrangement of prototype Delta aircraft structure.

Stages in the construction of a typical component may be followed by reference to Fig. 7. A piece of Xylonite sheet was cut out and placed between the hot alloy tools; these tools were pressed together to form the stiffening flutes while at the same time the assembly was pressed into a block of hard rubber in order to form the flanges. Component parts of one rib are shown ready for assembly and the final assembly, in which the parts have been cemented together with Halac Solution (amyl acetate 40 per cent., acetone 60 per cent.), can also be seen. Simple ribs and similar parts were formed by means of a male tool and a rubber bolster in an exactly similar way to that used for the manufacture of the full-scale metal components.

Figure 8 shows most of the tools and jigs required for the manufacture and assembly of the wing tips and elevons.

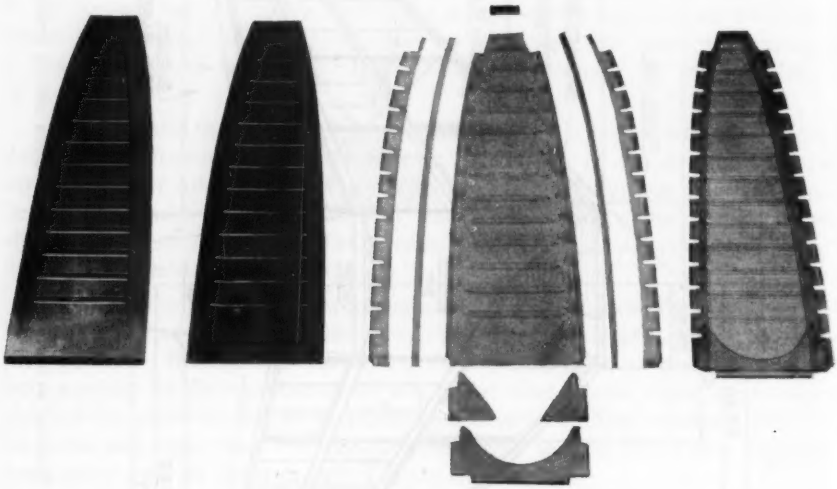

Fig. 7.
Stages in the construction of a Xylonite wing rib.

Considerable care had to be exercised in the cementing process, but provided that an artist's fine paint brush is used and the quantity of Halac solution used is kept to a minimum, a strong joint can be obtained. In some cases parts were cemented along a continuous line, but where it was necessary to reproduce the effect of a bolted joint, a small hole was drilled in one of the parts to be joined and a small quantity of the cementing solution was applied to the hole. Skill and experience are necessary to ensure that the structure is not distorted during the cementing process, and that the Xylonite is not dissolved by applying too much cementing solution.

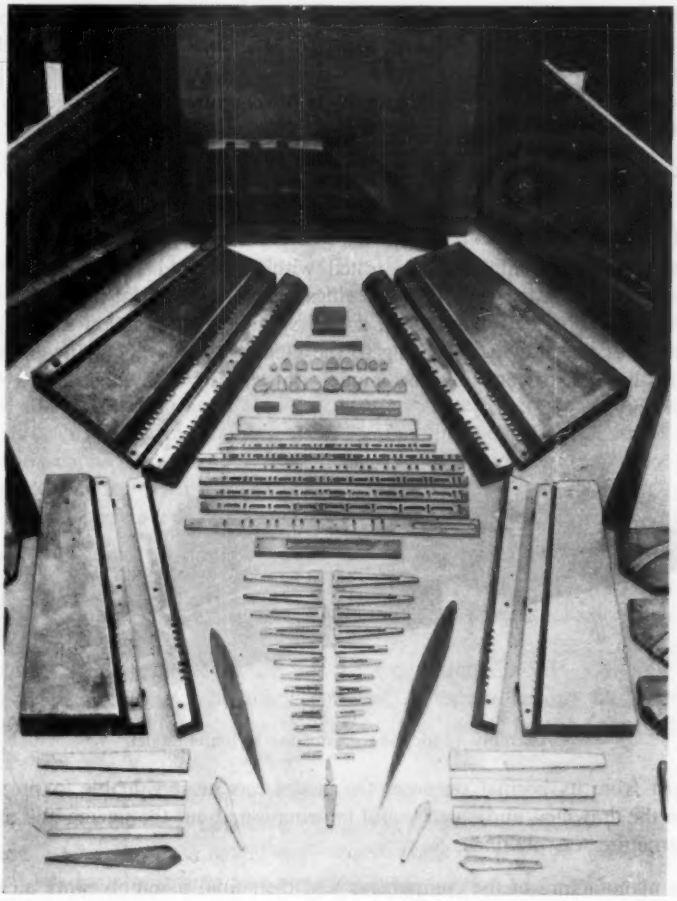

Fig. 8.

Most of the tools and jigs required for the manufacture and assembly of wing tips and elevons.

3.3. *Assembly of the model*

After the completion of the sub-assemblies, the main wing and fuselage assemblies were started.

The wing was assembled in a wooden cradle jig which is shown in Fig. 9. It is of interest that an identical form of jig was used later for the construction of

the full-scale wing. The wing skins, which were previously moulded to shape, were laid in the jig and the internal stringer-spar-rib structure built into it. Fuel tanks, undercarriage and items of equipment were mounted at the appropriate stage and the structure finally completed. The method of assembly at each stage was almost identical to that which was subsequently used for the full-scale wing.

The assembly of the fuselage followed on similar lines.

3.4. *Time for construction of the model*

The model was completed and tested within two and a half years. As the model was built from the prototype drawings, this time does not represent the time needed to build a model of this type, as the speed of construction was dependent on the issue of the drawings. Owing to the facility whereby Xylonite models can be built, the construction of the model outstripped the construction of the actual prototype.

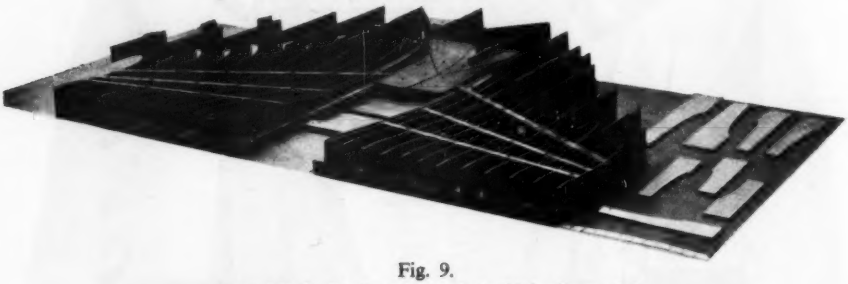

Fig. 9.
Assembly jig for the wings of the Xylonite model.

Apart from its normal purpose, the model was most valuable in providing a check on the drawings, and much useful information about the jigging and assembly of the structure was obtained.

The manufacture of the components and their final assembly were all done in one laboratory, which was situated alongside the laboratory which was used for the tests. The temperature of the test laboratory was kept constant at 65°F. Thus, with the exception of the wind-tunnel tests, the model spent its complete life in one environment.

4. The Stiffness Tests

It was necessary to measure the flexural and torsional stiffness of the model, and also the torsional stiffness of the elevon in order to calculate the theoretical flutter speeds of the model for comparison with the observed values to be obtained from wind-tunnel tests on the model.

The experimental model stiffnesses can also be converted easily to full-scale values, so that a comparison can be made between the deduced values for the full-scale wing and the actual values from full-scale tests. This comparison is made together with the theoretical stiffness.

In addition, the comparison between the port and starboard model wing stiffnesses gives an indication of the consistency to which the wings have been built.

4.1. *Stiffness test procedure*

For both the wing flexure and wing torsion tests the model was mounted in an inverted attitude. It was held to the rig by means of the four attachment lugs at both the rear spar frame and the leading edge frame. The tips and elevons were not attached for these tests. Contour boards were mounted at the four measuring stations on each wing and provision was made for attaching dial gauges at each of these stations as well as at the wing roots. There was provision for three dial gauges at each section, the stations being 35 per cent., 60 per cent. and 80 per cent. of the wing chord. Simple tests were made first to ensure that the contour boards did not add any apparent stiffness to the wings, and that the undercarriage doors were not load-carrying. These tests consisted of measuring the stiffnesses at an outboard station with, and without, the inner contour boards fitted and with, and without, the undercarriage doors in position.

For all stiffness tests, the loading and measuring stations considered were along chord lines, which are themselves parallel to the direction of flight. Throughout all the stiffness tests, the temperature was kept constant at 65°F. Although it was not possible to keep the humidity constant, a careful record was kept of the humidity and temperature during the tests. The humidity values recorded were all in the range from 55 to 70 per cent.

While the stiffness tests were being done, the Young's modulus values for a set of tensile specimens were measured. These tests followed the procedure outlined in Section 2.3.2. Both the model tests and the tensile tests were done in the same room so that the temperature and humidity were the same for each.

4.1.1. *Symmetrical torsion tests*

In the symmetrical torsion tests a nose-up torque was applied symmetrically to each wing simultaneously and for each loading station the twists, and the points about which they occurred, were measured at all five stations on each wing. This arrangement is shown in Fig. 10.

As each increment of load was applied, a time of two minutes was allowed to elapse before any recordings were made. This was to produce agreement with the tensile specimen calibrations for Young's modulus and also to permit most of the creep to occur before taking readings.

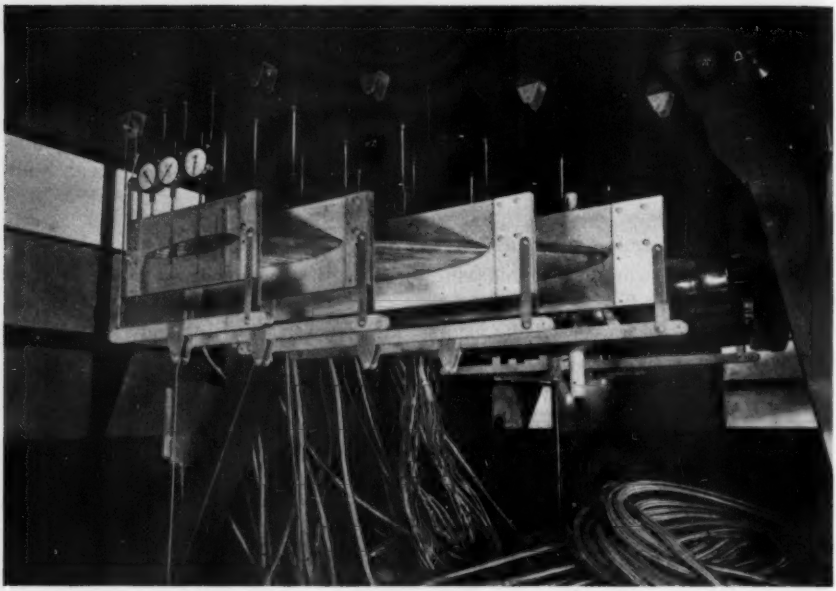

Fig. 10.
Model rigged for wing torsional stiffness tests.

4.1.2. *Asymmetric torsion tests*

A few check tests in which the torsion loads were applied asymmetrically, showed that there was no significant difference between the symmetric and asymmetric torsion properties.

4.1.3. *Flexure tests*

In the flexure tests, a positive flexure load was applied simultaneously to each wing at a chosen position on each loading section, in such a way that no twist occurred at these sections. For each loading station the deflections and twists were measured at all five stations on each wing. Here, as in the torsion tests, a two minute interval was observed between the loading and reading of the dial gauges.

4.1.4. *Elevon stiffness measurements*

In order to measure elevon stiffness, an elevon was held rigidly at its root by means of the torque tube, and torques were applied by means of a contour board at the 90 per cent. span station. The twists were measured at the loading station and at four other stations farther inboard by means of a mirror, scale and telescope system.

4.2. *Stiffness results*

For the model wing torsion tests, the percentage chord at the loading station about which the twist occurred is given in Table II.

TABLE II

Values of percentage chord. Torsion tests.

Station (in.)	5.49	11.71	17.21	23.58	27.89
Port wing	42	30	14	−15	−54
Starboard wing	42	32	14	−12	−56

For the model wing flexure tests, the percentage chord at the loading station at which the load was applied in order to produce no twist at that station is given in Table III.

TABLE III

Value of percentage chord. Flexure tests.

Station (in.)	11.71	17.21	23.58	27.89
Port wing	26.3	20.3	15.1	4.6
Starboard wing	28.1	21.0	14.0	8.1

To convert the model stiffnesses to the full scale stiffnesses, the following two factors are deduced.

(*i*) Torque per unit twist is proportional to $I^2 Et$ and therefore

$$\text{Torsional stiffness factor} = (l_F^2/l_M^2)(E_F/E_M)(t_F/t_M)$$

$$= 5.378^2 \times (10/0.35) \times 2.56$$

$$= 2{,}115,$$

(since $E_F = 10 \times 10^6$ lb./in.^{2}, $E_M = 0.35 \times 10^6$ lb./in.^{2}, $t_F/t_M = 2.56$ and $l_F/l_M = 5.378$). It has been assumed that Poisson's ratio is the same for both Xylonite and aluminium alloy.

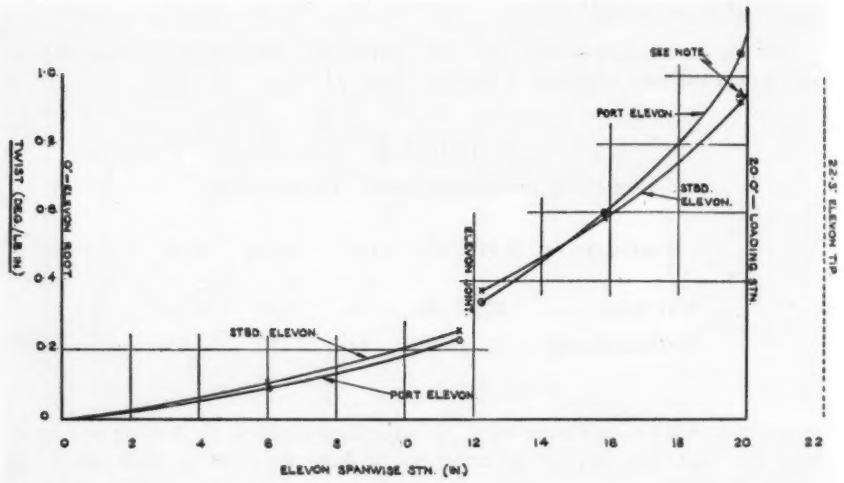

Fig. 11.

Model elevon torsional stiffness.
Loading at 0.9 span (parallel to direction of flight).

△ Experimental value measured at loading station deduced from full-scale elevon tests.

(*ii*) Load per unit deflection is proportional to Et and therefore

$$\textit{Flexural stiffness factor} = (E_F/E_M)(t_F/t_M)$$

$$= (10/0.35) \times 2.56$$

$$= 73.1.$$

Figure 11 gives the results of the elevon torsion tests together with a point derived from measurements on a full-scale elevon. It is seen that the agreement is good.

A comparison of the wing stiffness results for the full-scale aircraft, the values deduced from the model, and the theoretical values is given in Figs. 12 to 15 inclusive. In these figures, all values are referred to wing roots.

It can be seen from these figures that the stiffness comparisons show the values deduced from the model to be stiffer in both flexure and torsion than the full-scale aircraft by about 10 per cent. This can be considered quite satisfactory when it can be seen, on both the model and the full-scale aircraft, that the variation between port and starboard wings, which theoretically should be identical, may be as large as 5 per cent.

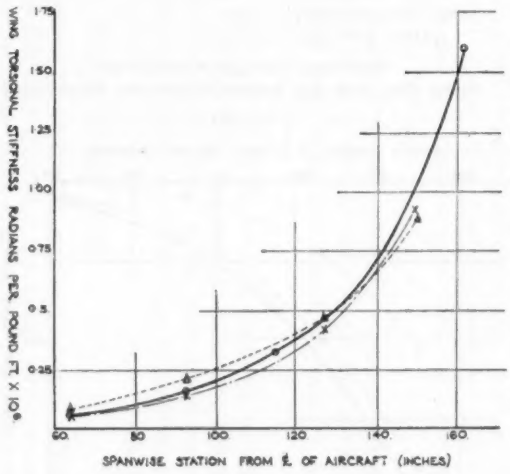

Fig. 12.

Comparison between calculated, full scale, and model wing torsional stiffness: Port wing.

———— Full scale aircraft
— - — - — Deduced from model
- - - - - - - - - - Calculated

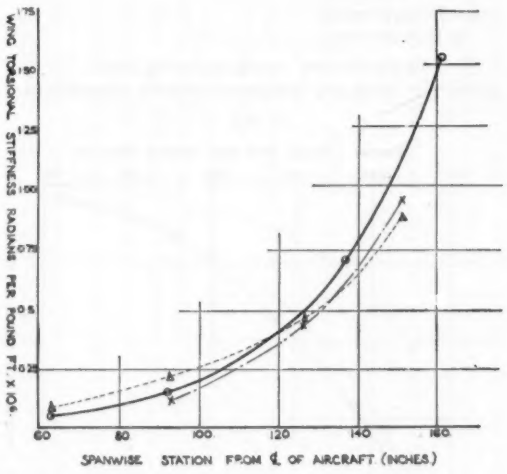

Fig. 13.

Comparison between calculated, full scale, and model wing torsional stiffness: Starboard wing.

———— Full scale aircraft
— - — - — Deduced from model
- - - - - - - - - - Calculated

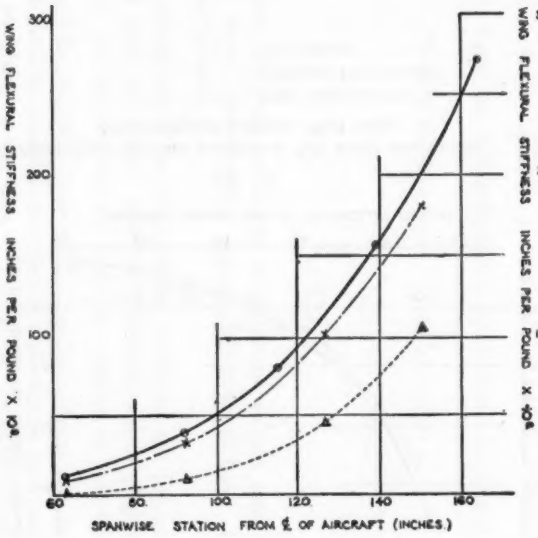

Fig. 14.

Comparison between calculated, full scale, and model wing flexural stiffness: Port wing.

———— Full scale aircraft
— - — - — Deduced from model
---------- Calculated

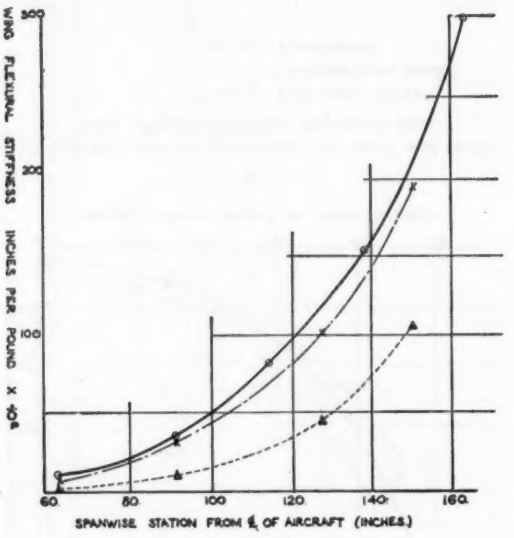

Fig. 15.

Comparison between calculated, full scale, and model wing flexural stiffness: Starboard wing.

———— Full scale aircraft
— - — - — Deduced from model
---------- Calculated

The following two factors may account for at least part of the stiffness variation between the full-scale aircraft values and those deduced from the model.

(*a*) In order to convert the measured model values to full-scale dimensions, a modulus of elasticity of 10×10^6 lb./in.^{2} has been assumed for aluminium alloy and 0.35×10^6 lb./in.^{2} for Xylonite. This value for Xylonite has been carefully chosen in the light of tests on control specimens. The value for aluminium alloy has been chosen because it is thought to be an average value. However, Howarth[11] gives an average modulus of 9.6×10^6 lb./in.^{2} for D.T.D. 610. The use of too high a value for the modulus of elasticity of the aluminium alloy would have the effect of making the wing stiffness as deduced from the model, too stiff. For the values in question, the deduced model stiffness would be too high by about four per cent.

(*b*) It has been assumed for both the model and the full-scale aircraft that the actual material sheet thicknesses are the nominal values. Inspection records show that the sheets of aluminium alloy and Xylonite are on the average one per cent. and five per cent. above nominal respectively. This would account for an increase of four per cent. in the stiffness of the model.

Thus the two effects together could account for the stiffness as deduced from the model being eight per cent. greater than that determined from the full-scale aircraft.

The theoretical torsional stiffness values agree reasonably well with both sets of experimental values. The apparent reduction in theoretical torsional stiffness towards the root is probably due to neglecting the effects of root constraint and differential spar bending.

The theoretical flexural stiffness is somewhat greater than the experimental values, but it must be remembered that the calculated value assumes the wing to be rigid at the root. If an approximate allowance is made for this difference the agreement is much closer.

The twists of the wing sections occurring during flexure tests were also measured, although it was not possible to achieve this very accurately due to the small angles involved. These results were used to estimate the locus of flexural centres which was found to be very close to the front spar at 35 per cent. chord.

5. The Strain Gauge Tests

Because of the unorthodox type of wing used on the full-scale delta aircraft it was found that little theoretical knowledge was available on the stresses in such wings, and therefore some experimental results were required to augment the theoretical data. For this purpose it was necessary to install strain gauges upon the Xylonite model of the aircraft and to obtain the model stress distributions corresponding to the applied loading cases.

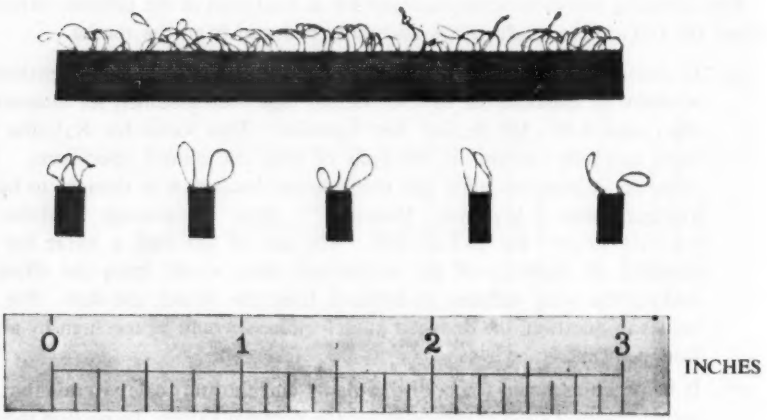

Fig. 16.
Miniature type woven strain gauge.

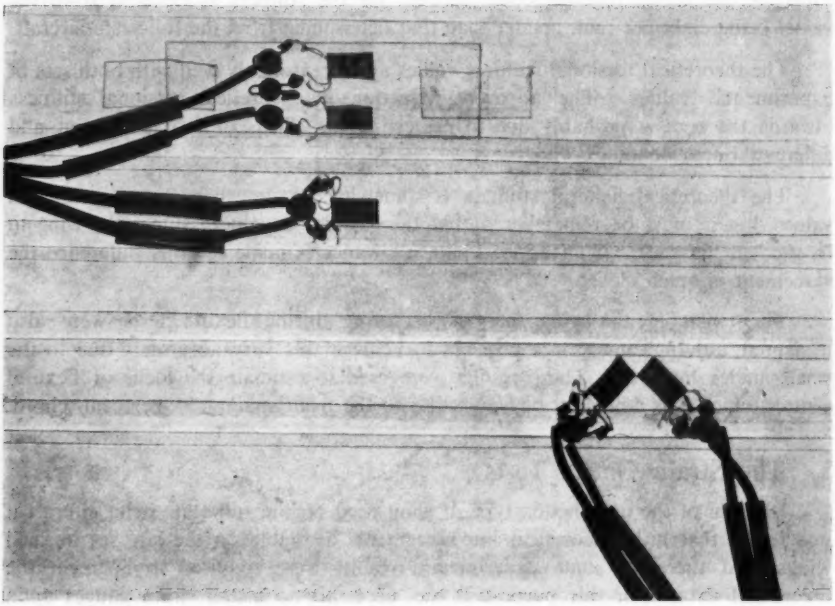

Fig. 17.
Typical shear and direct strain gauge installations.

The first difficulty encountered was in finding an electrical resistance strain gauge of sufficiently small dimensions, the only one available being the 0.25 in. × 0.125 in. British Celanese woven gauge, which had been the subject of research and development with Boulton Paul Aircraft Ltd. for some years. During this time a suitable technique was evolved for mounting, recording and calibrating the gauges.

Two loading cases were considered: first, the case "B" loading corresponding to high wing loading at high speed, in which the stress distribution at the wing root was required; second, an undercarriage loading case in which the stress diffusion into the neighbouring structure was needed. In all, 230 strain gauge stations were used, involving the installation of some 920 strain gauges on the model.

5.1. *The miniature strain gauge*

The miniature strain gauges were woven by British Celanese Limited. The weft consisted of 0.001 in. silk covered Advance resistance wire and the warp consisted of silk alone. The gauges were woven as a continuous ribbon 0.25 in. in width with 100 picks to the inch, the wire being unbroken throughout the length of tape. This wire was brought out at alternately 8 and 4 picks to form a loop with the adjacent pick. The active part of one gauge consisted of the 8 picks and the loop at each end, and it was formed by cutting the ribbon at the narrow, 4 pick, loop spacing. The overall dimension of the gauge thus formed was 0.25 in. × 0.125 in. and the loop length was 0.25 in. Fig. 16 shows a piece of uncut gauge ribbon and also the single gauges formed by cutting.

Before the gauge was mounted, the silk had to be removed from the loops; a method as satisfactory as any consisted of carefully scraping the loops with a razor blade. For mounting on Xylonite, the adhesive used was Halac solution, a mixture of amyl acetate and acetone, and for joining the gauge leads to the loops soldering was quite satisfactory provided that care was taken, and a non-corrosive flux was used. It was found necessary to hold the leads firmly, close to the gauge after jointing, to ensure that the weight of the leads would not break the loops. For this purpose Xylonite pegs were used, and a satisfactory scheme was devised whereby the leads to a pair of gauges, one on each side of the skin, were mounted on a single piece of 3 mm. Xylonite rod fixed to the adjacent structure. The gauge leads were all brought away on the one side of the skin through small holes. (*See* Fig. 17.)

The gauges had a mean resistance of 65 ohms, and a mean sensitivity factor of approximately 1.0. The gauge current was between 12 and 16 milliamps.

5.2. *The strain gauge testing procedure*

Considerable care had to be taken in order to ensure reliable results in the use of the miniature electric strain gauges, and this section deals with the testing procedure adopted in the tests on the Xylonite model.

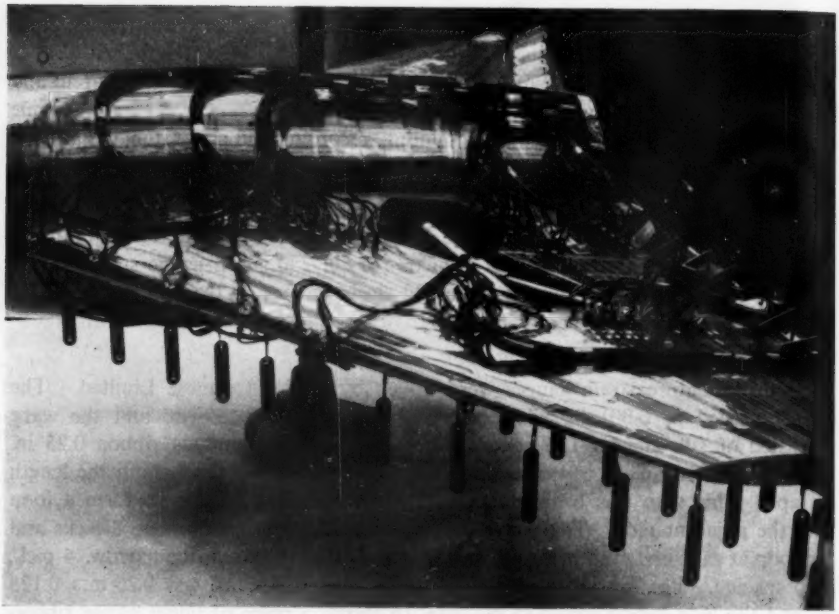

Fig. 18.
Model, with strain gauges attached, before mounting in the test frame.

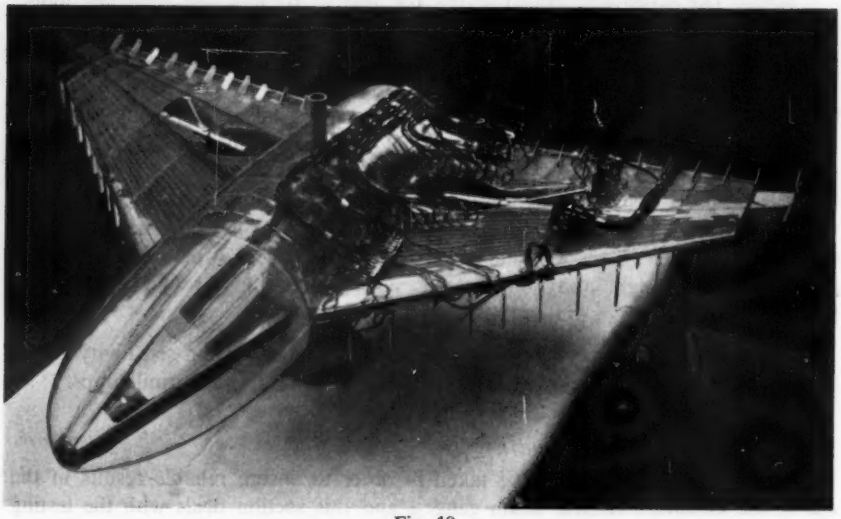

Fig. 19.
Model, with strain gauges attached, before mounting in the test frame.

The ribbon was first cut into individual gauges, and each ten or twelve gauges formed a batch. One gauge from each batch was then mounted on a calibration beam and its resistance and sensitivity factor were measured. The results showed that in all cases the resistance values were consistent, and that only one serious deviation in the sensitivity factors was found. One length of ribbon of several feet had a gauge sensitivity factor of only 30 per cent. of the other lengths of ribbon, this being found to be due to faulty weaving. This length was rejected. The remaining gauges from the batches were then mounted upon the model as described in Section 5.1, the gauges being mounted on each side of the skin at each station; the resistance of each gauge was then checked to ensure that the soldered joints were satisfactory.

When all the strain gauges were installed (Figs. 18 and 19) the model was mounted in the testing frame in the same room as the calibration equipment, and the room was kept at a constant temperature of 65°F. The calibration equipment consisted of a Xylonite beam upon which eight calibration gauges were mounted. The beam was subjected to a pure bending moment. The deflection of the beam was measured by a vernier microscope, and another eight calibration gauges mounted upon an unstrained Xylonite beam were placed alongside the strained beam to provide for temperature compensation. An accurately calibrated potentiometer was used in a null method circuit for measuring the strain sensitivity factor. When not undergoing a test the calibration beams were carefully housed in a rack adjacent to the calibration equipment.

The leads from the strain gauges mounted on the model were all cut to a length of six feet so that their resistance was uniform; these leads were attached to junction boxes mounted alongside the model test rig (Fig. 20).

From these junction boxes, metal-braided multi-core cables ran to the recording equipment, which was of Boulton Paul construction capable of recording 168 strain gauge stations in ten seconds. The strain gauge signals from the cathode ray oscilloscope were photographically recorded and calibration signals were switched in between every seven gauge stations. A schematic diagram of the high-speed strain measurement set is shown in Fig. 21.

During the time at which the tests on the model were being done, the calibration beams were each in turn placed in the calibration rig and the sensitivity factor of each gauge was accurately measured, both in tension and compression, although the difference in the sensitivity factor between the two cases was very small.

For each of the loading cases considered, the load was applied to the model in several increments and after each increment had been applied, two minutes were allowed to elapse before the strains were measured. This brought the tests into line with the measurement of Young's modulus by applied tension loading.

The stiffening effect of the miniature strain gauge used was very small, but it was measured approximately, and its effect was taken into account. When tensile

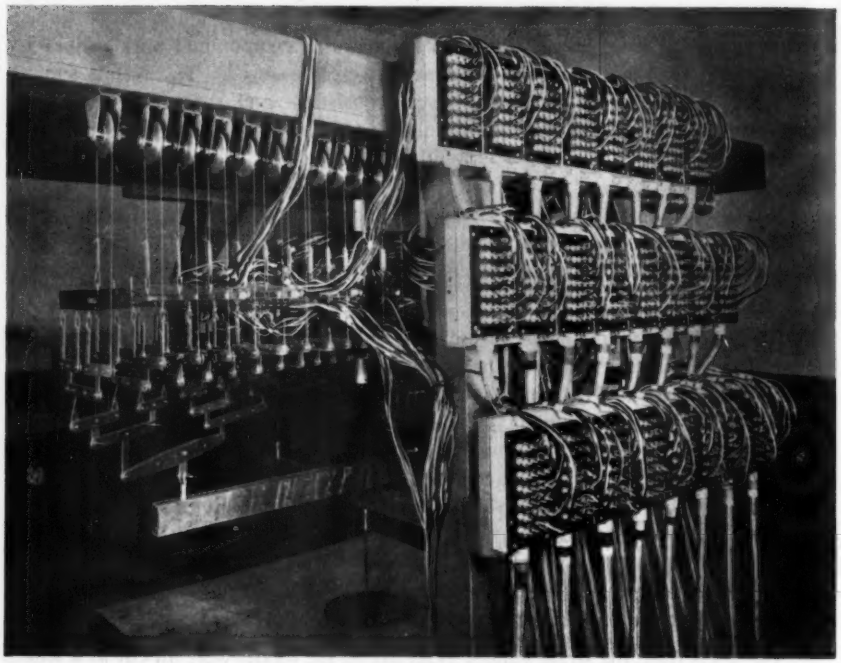

Fig. 20.
Model in test frame showing strain gauge junction boxes.

specimens were covered on both sides with these miniature strain gauges, an average increase in Young's modulus of five per cent. was measured, for tensile specimens 0.030 in. thick. From this value the stiffening effect can be estimated for sheets of other thicknesses.

5.3. *Case "B" loading*

Case "B" loading corresponded to a high normal acceleration at a high speed. On each wing the load was applied through Xylonite pegs glued to the wing at spar-rib junctions. There were 48 loading points on each wing, four on each of 12 chords. An additional loading point was used to represent the inertia relief due to the engine, and all these 97 loading points were linked together as shown in Fig. 20.

The model was mounted in an inverted position, therefore the positive lift loads were applied downwards, while the row of negative lift loads along the rear spar were applied by cables passing over a set or pulleys before being linked with the positive loads. The elevons were not in position for these tests and only dummy wing tips were used; the purpose of the dummy wing tips was to provide attachment

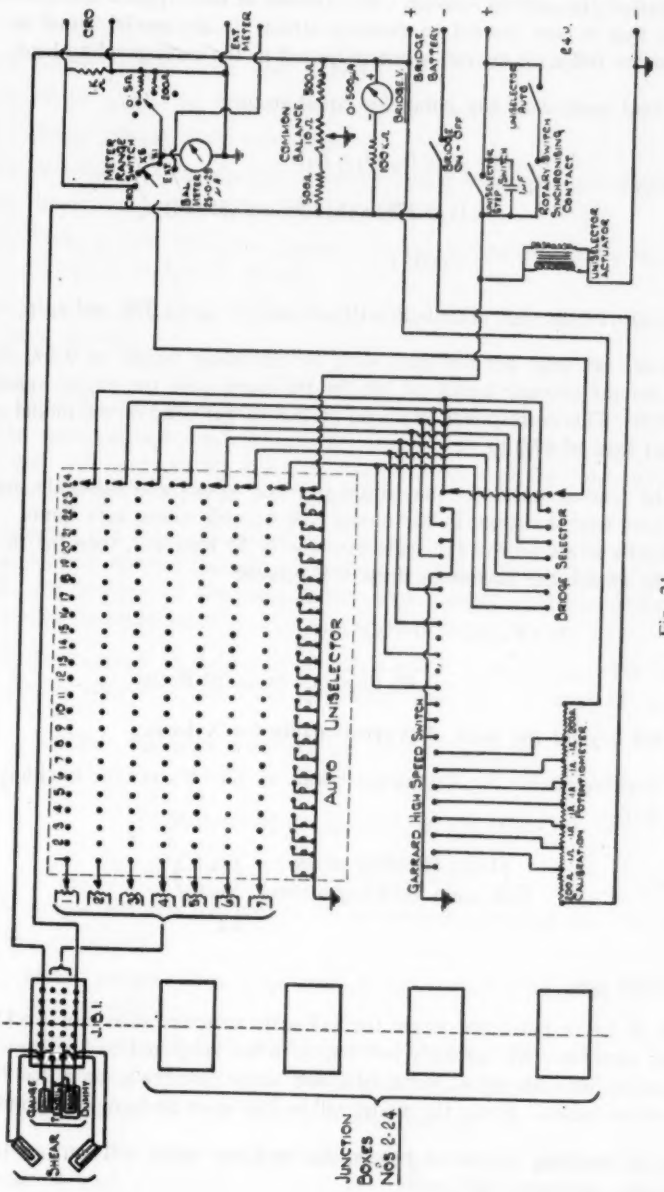

Fig. 21.
Schematic diagram of high-speed strain measurement set.

points for part of the applied loading. The amount of load applied was determined by the fact that it was desired to produce strains in the model equal to those produced in the full-scale aircraft when subjected to the corresponding loads.

If P = load applied at any point, for equal strains

$$P_M/P_F = l_M t_M E_M/(l_F t_F E_F)$$

$$= (1/5.378) \times (1/2.56) \times (0.35/10)$$

$$= 0.00254.$$

(since $E_F = 10 \times 10^6$ lb./in.^{2}, $E_M = 0.35 \times 10^6$ lb./in.^{2}, $l_F/l_M = 5.378$ and $t_F/t_M = 2.56$).

The total net load per full-scale wing for an all-up weight of 9,500 lb. was 19,250 lb. for an ultimate factor of 10; for the same case the engine relief load was 18,600 lb. This corresponds to a load of 48.9 lb. per wing on the model and an engine relief load of 47.2 lb.

For the loading case of equal strain in both model and full-scale machine, it can be seen that the stress in the model will be well within safe limits. If the ultimate tensile stress on the full-scale machine is 30 tons/in.^{2}, then for the same strain in the model, the maximum stress will become

$$30 \times E_M/E_F = 30 \times 0.35/10$$

$$= 1.05 \text{ tons/in.}^2 \text{ or } 2{,}350 \text{ lb./in.}^2$$

which is not beyond the limit of proportionality for Xylonite.

The buckling stress for flat panels varies as $E(t/l)^2$, or, the buckling strain varies as $(t/l)^2$.

Hence,
$$\frac{\text{Model buckling strain}}{\text{Full scale buckling strain}} = \left(\frac{t_M l_F}{t_F l_M}\right)^2$$

$$= 4.4$$

in the present case.

Thus, if for a particular strain the full-scale structure does not buckle, then the model structure will certainly not buckle when subjected to the same strain. All the major full-scale skins, webs, ribs, and so on, are thick, such that buckling corresponds to failure. Hence the model will be free from buckling when under load.

For the buckling of curved panels, the buckling strain will vary as (t/l) and the foregoing argument still holds.

The gauges that were recorded in the Case "B" loading were positioned principally as follows:—

(*a*) Direct gauges along spar booms.

(*b*) Shear gauges in skin adjacent to spar booms.

(*c*) Shear gauges along spar webs.

(*d*) Rosettes in skin adjacent to body between front spar and leading edge.

(*e*) Shear gauges along leading edge.

(*f*) Shear gauges and direct gauges on skin of wing portion through the body, along centre line of aircraft.

A total of 168 gauge stations was recorded in this case, for each of six increments of load.

5.4. *Undercarriage loading*

The undercarriage loading case corresponds to a vertical load through the wheel hub with the aircraft in a tail down attitude and the oleo strut one third closed. No drag or side load was included.

To apply this load, the model was mounted as in Section 5.3 and the undercarriage loading applied through a structure similar to that used on the full-scale aircraft, and attached to the wing in the same manner. Both undercarriage legs were loaded simultaneously.

The load applied to the model was that which would produce the same strain as in the full-scale structure when the aircraft load is 3.75 times the static value.

$$\text{Thus, full scale load per leg} = (9{,}500/2) \times 3.75$$
$$= 17{,}800 \text{ lb.}$$
$$\text{Model load per leg} = 17{,}800 \times 0.00254$$
$$= 45.2 \text{ lb.}$$

The gauges that were recorded in the undercarriage loading case were positioned principally as follows:—

(*a*) Direct gauges along front and centre spar booms adjacent to undercarriage rib.

(*b*) Shear gauges on wing skins adjacent to undercarriage rib.

(*c*) Shear gauges on front and centre spar webs adjacent to undercarriage rib.

(*d*) Shear gauges on nose portion of undercarriage rib.

A total of 60 gauge stations was recorded in this case for each of six increments of load.

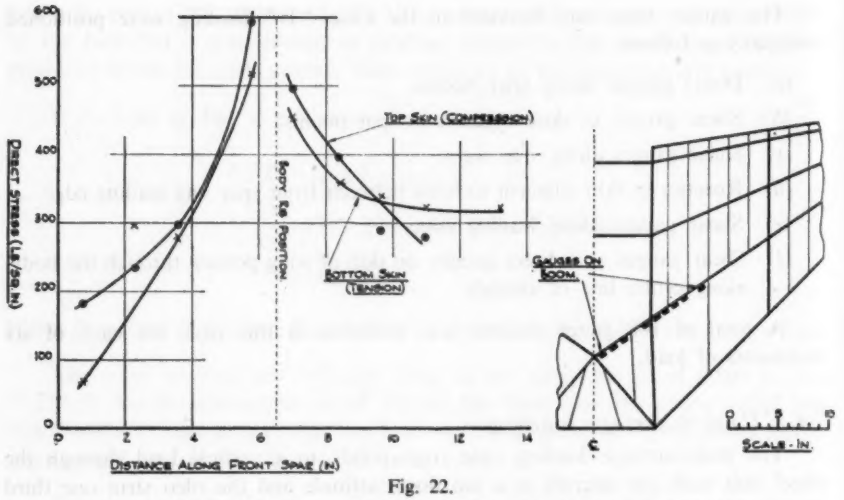

Fig. 22.

Case " B " loading. Direct stress in front spar boom (flange).

5.5. *Strain gauge results*

The results of the strain gauge tests were analysed by projecting the film of the cathode ray oscilloscope trace and reducing the deflections to resistance changes. The strains were obtained by taking a mean gauge sensitivity of 0.91 and the model stresses were derived by using a value of Young's modulus of 0.35×10^6 lb./in.^{2} An allowance was made for the stiffening effect of the gauges, which was found to

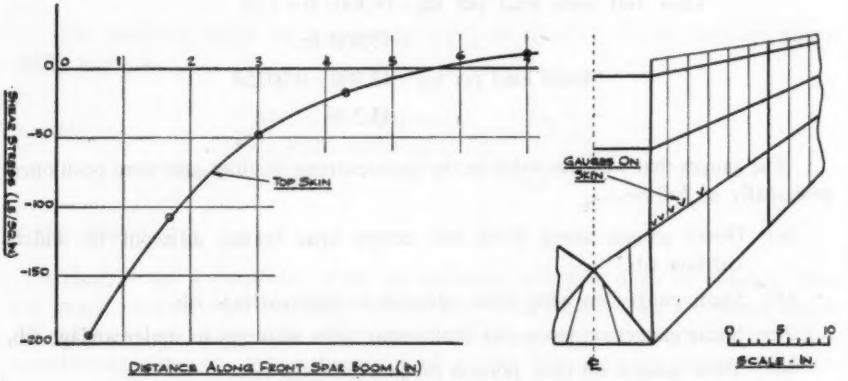

Fig. 23.

Case " B " loading. Shear stress in wing skin aft of front spar.
(A positive shear corresponds to a nose up torque applied outboard of the gauge.)

be about 5 per cent. for a piece of 0.030 in. Xylonite with one gauge on each side. The mean resistance of the gauges was 65.8 ohms with a standard deviation of 1.1 ohms. The standard deviation of the sensitivity factor was found to be 0.049.

It is of interest to note that when the gauges were recorded only 3 stations out of a total of 228 were found to be inoperative.

In nearly all cases the linearity of the strain-load relationship for each gauge station was good. Typical distributions of the stresses in the model are as shown in Figs. 22, 23 and 24. Fig. 22 gives the diffusion of end load into the front spar boom. Outboard of the body line the end load diffuses from the skin between the front spar and the centre spar into the front spar boom, whereas inboard of the body line the end load diffuses from the boom into the skin of the torsion box.

The distribution of shear stress in the wing skin just aft of the front spar is plotted in Fig. 23. The distribution of the shear stress in the centre spar web is given in Fig. 24.

A calculation was made in order to verify that the bending moment in the wing at the body line was equal to the applied bending moment due to Case "B" loading. This calculation actually gave a bending moment in the body that was 11 per cent. less than the applied bending moment. There are three reasons for this apparent difference.

(*i*) Some difficulty was encountered in the calculation owing to the difference in "angle of sweepback" of the stringers and spars.

(*ii*) In all cases "nominal" skin gauge sizes were used and not the actual sizes. Generally speaking, the actual gauge sizes are about 3 per cent. greater than the nominal values.

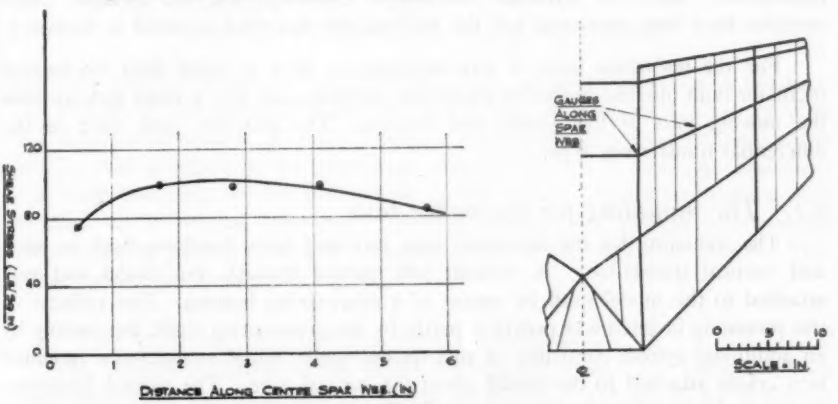

Fig. 24.
Case "B" loading. Shear stress in centre spar web.
(A positive shear corresponds to an up load on web applied outboard of the gauge.)

(*iii*) It was assumed in the calculations that no load whatsoever passed from the wing skin into the body between the front and centre spars, and between the centre and rear spars.

In no cases did the experimental results show a weakness in the model structure and the information obtained was sufficient to confirm the basic assumptions made in the full-scale stressing, since the strain gauge results and the calculated stresses agree quite closely except in the case of stresses in which root constraint and shear lag play a large part.

6. The Resonance Tests

Having completed the stiffness and strain gauge tests on the Xylonite model, it had been decided to carry out resonance and flutter tests on the same model. The type of mounting required for the flutter tests had a considerable effect on the mounting for resonance tests and also on the actual tests made.

It was decided that only symmetrical vibrations would be considered; therefore the model required two degrees of freedom, those of pitch and vertical translation. In addition, a dummy nose and tail would be required for tunnel tests; these were suitably mass-balanced and provision was made for varying the mass, to cater for a suitable centre of gravity range.

The principal difference between the resonance and flutter tests and the stiffness and strain gauge measurements is that the former are dynamic, and the latter static, tests. This means that since Xylonite has both static and dynamic physical properties, accurate values for the dynamic moduli must be available in order to convert the model resonance frequencies and flutter speeds to the full scale equivalents. Both the dynamic modulus of elasticity, and the dynamic shear modulus have been measured and the methods are described in detail in Section 2.

For the resonance tests, it was necessary to have a small light mechanical oscillator built into the model for excitation purposes and also a small pick-up with the moving part of low inertia and friction. The pick-ups used were of the differential transformer type.

6.1. *The mounting for resonance tests*

The mounting for the resonance tests provided body freedoms both in pitch and vertical translation. A vertical tube passed through the model and was attached to the model itself by means of a cross-spring bearing. The stiffness of this mounting in pitch was provided partly by the cross-spring itself, but mainly by an additional system consisting of two springs under initial compression mounted in a cradle attached to the model about the vertical tube. The natural frequency of the model in pitch was about four cycles per second.

The vertical tube itself formed the shorter parallel side of a symmetrical

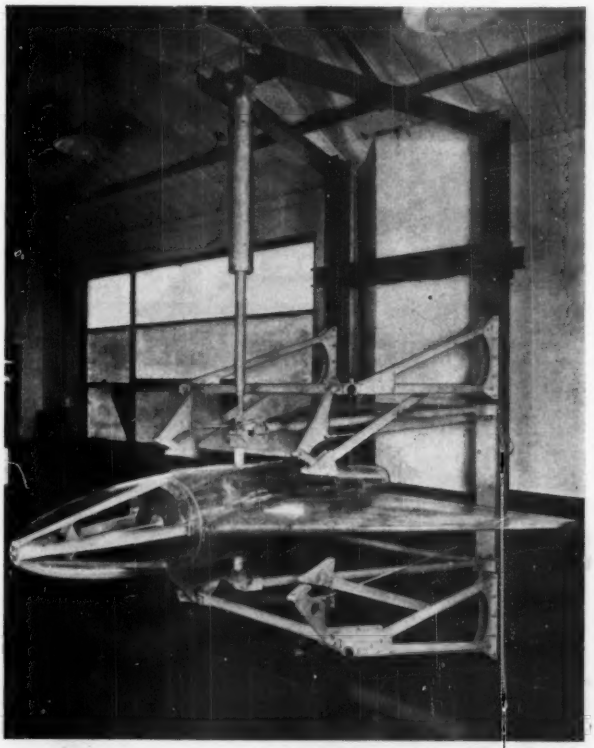

Fig. 25.
Model rigged as for flutter tests. Grab in " off " position.

trapezium linkage system, in which all the joints contained cross-spring bearings. This linkage system provided model freedom in vertical translation. The purpose of a trapezoidal system, as distinct from a rectangular one, was to provide the stability that is absent in the latter type, since the system as used was equivalent to a sting mounting pivoted well ahead of the model. Additional stiffness was provided by a vertical attachment working against two springs under initial compression to provide a natural frequency of about five cycles per second. This linkage system can be seen in Fig. 25.

6.2. *The recording equipment for resonance tests*

The vertical excitation of the model for resonance tests was produced by a small mechanical oscillator mounted inside the fuselage, and driven by a flexible drive from a Shrage type variable speed motor. The static out of balance of the vibrator was 1.3 ounce inches.

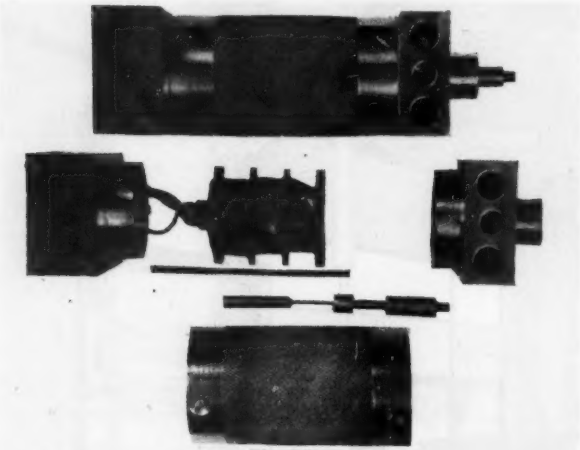

Fig. 26.
Boulton Paul differential transformer type pick-up.

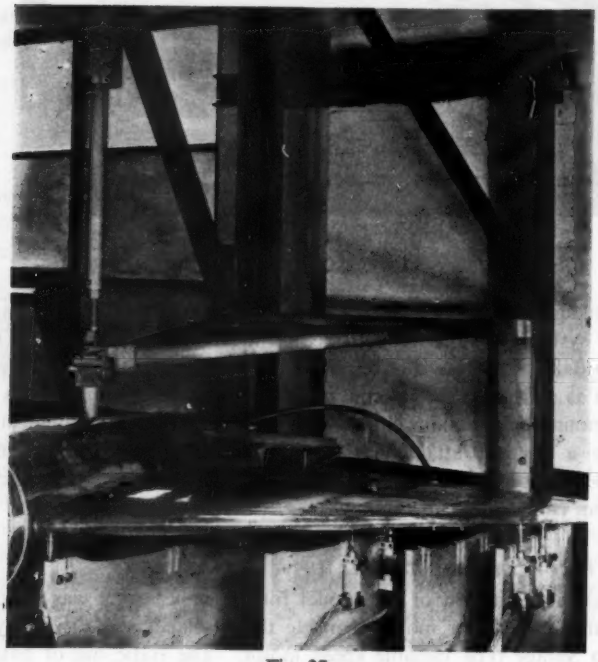

Fig. 27.
View of model showing pick-ups in position.

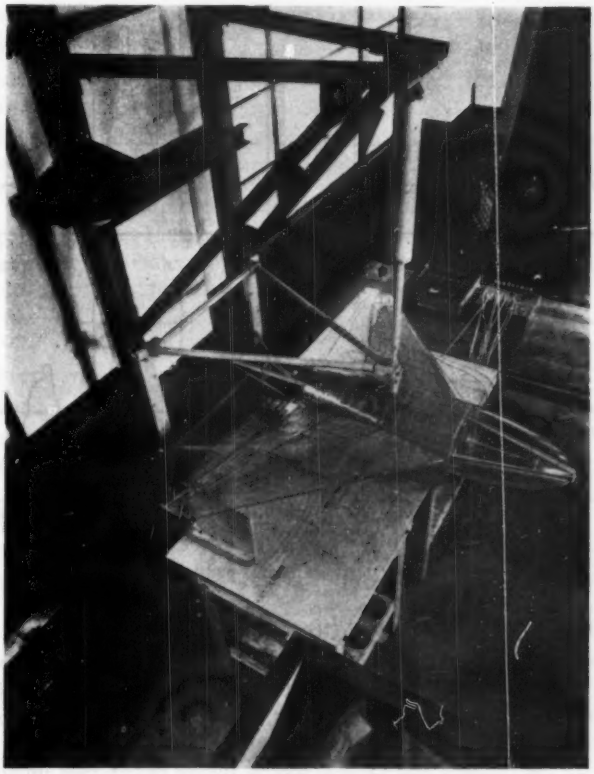

Fig. 28.
General view of model during resonance tests.

The pick-ups used for recording the displacement amplitudes and frequencies of the model were of the Boulton Paul differential transformer type, a displacement pick-up. These pick-ups have the advantage that the weight of the moving part is very small (about 5 gm.) and that they are virtually frictionless. The sensitivity of these pick-ups is 20 volts per inch, the maximum displacement being 0.1 in. to each side of the balanced position; an exploded view is shown in Fig. 26. A view of the model with some pick-ups in position is given in Fig. 27.

The signals from the pick-ups were photographically recorded on a 10-channel Boulton Paul recorder in which eight channels were used for pick-ups and the remaining two channels were used for a 50-cycle trace and a calibration signal. From the film, both the amplitude of vibration and the phase relation were obtained. A general view of the model, pick-ups and recording gear is shown in Fig. 28.

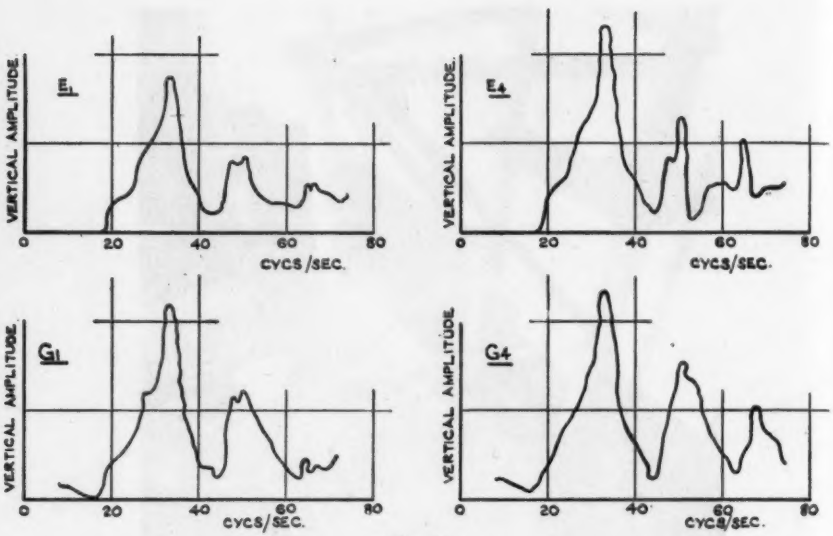

Fig. 29.
Resonance tests. General panorama.

6.3. *The resonance test procedure*

The procedure adopted for the model resonance tests followed as nearly as possible that for full-scale tests. First, using four pick-ups only, two on each tip, the amplitudes of vibration were examined over a range of frequencies from 8 to 75 cycles per second. The modes were then examined in detail, the elevon tests being made both with the inboard end locked, representative of the case involving power controls, and also with the inboard end restrained by a spring of appropriate stiffness corresponding to manual operation. For all the resonance tests, the elevons were 70 per cent. mass balanced as on the full-scale aircraft, and the model centre of gravity was at the forward limit, 48 per cent. chord, the fuel tanks being empty.

6.4. *Resonance test results*

6.4.1. *Model results*

The results obtained from the resonance tests are shown in Figs. 29 to 32 inclusive. Fig. 29 gives the general panorama, showing peaks at 33.4, 51.1 and 67.4 cycles per second. The mode analysis for the 33.4 cycles/sec. resonance is shown in Fig. 30, that for the 51.1 cycles/sec. peak in Fig. 31, and that for the 67.4 cycles/sec. peak in Fig. 32. The nodal lines on the elevons in Figs. 30, 31 and 32 are for elevons with elastic constraint.

The first mode consists principally of flexure, the second mode of torsion,

flexure and body pitch, while the third mode appears to consist mainly of flexure and body pitch.

Towards the end of the resonance tests the model was found to be suffering slightly from fatigue and a loss in amplitude of the second mode was quite apparent. When the stiffness of the model was checked, a small reduction in torsional stiffness was detected, but there was no apparent change in the flexural stiffness.

While the resonance tests were being done it was observed that failures were occurring in the attachment of the mass balance to the elevon leading edge. On checking the stress calculations it was found necessary to reinforce these fittings on the full-scale aircraft, a fact that might have been overlooked had it not been for the model.

6.4.2. *Conversion to full-scale aircraft*

The resonance frequencies for the model can be converted easily to corresponding resonance frequencies for the full-scale aircraft, as follows:—

$$\omega_M/\omega_F = \{ E_{DM}\, t_M\, l_F^3/(E_{DF}\, t_F\, l_M^3) \}^{\frac{1}{2}},$$

and since $E_{DM} = 0.51 \times 10^6$ lb./in.^{2}

$$E_{DF} = 10.0 \times 10^6 \text{ lb./in.}^2$$

$$t_F/t_M = 2.56$$

$$l_F/l_M = 5.378,$$

$$\omega_M/\omega_F = \{ (0.51/10) \times (5.378)^3/2.56 \}^{\frac{1}{2}}$$

$$= 1.76.$$

Hence the corresponding full-scale resonance frequencies will be 19.0, 29.1 and 38.2 cycles per second.

6.4.3. *Comparison of model and full-scale resonance modes*

The model was tested over a range of frequencies from 8 to 75 cycles per second, which corresponds to a full-scale range of from 5 to just over 40 cycles per second. Three modes were found in this range on the model and three modes were found on the full-scale aircraft in the same range, the comparative frequencies being given in Table IV.

A comparison of the nodal lines for the first mode is presented in Fig. 30. It will be seen that the agreement between the model and the full scale is extremely good both in respect of the nodal line and the frequency of the mode.

The comparison of the second mode is shown in Fig. 31. Here the frequency agreement is again good, but the mode does not appear to be the same.

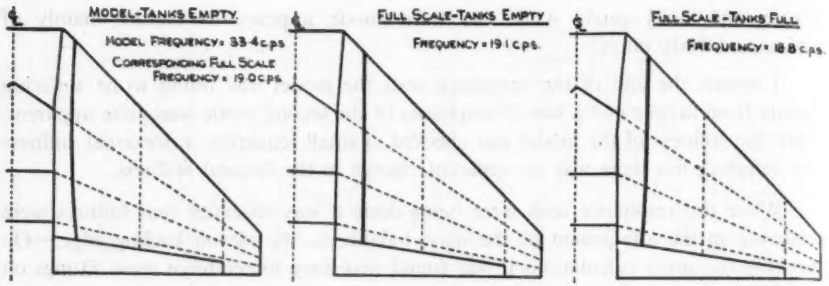
MODEL-TANKS EMPTY
MODEL FREQUENCY = 33·4 c.p.s.
CORRESPONDING FULL SCALE FREQUENCY = 19·0 c.p.s.
FULL SCALE-TANKS EMPTY
FREQUENCY = 19·1 c.p.s.
FULL SCALE-TANKS FULL
FREQUENCY = 18·8 c.p.s.

Fig. 30.
Resonant mode comparison.

The third mode comparison is given in Fig. 32. Here again the frequency agreement is good but the modes differ.

For the fundamental mode, the frequency and nodal line as predicted from the model is in extremely good agreement with the fundamental mode as measured on the full-scale aircraft. This shows that the basic idea of using Xylonite models to predict the full-scale resonance characteristics is quite sound, at any rate as far as the fundamental mode is concerned.

For the second mode, although the frequency agreement is good, the nodal line is not the same, but they both present a combination of torsion and flexure and if, in the case of the full-scale aircraft, a body pitching oscillation of wing resonance frequency is super-imposed, the derived full-scale wing nodal line is similar to that of the model. This is of considerable interest since, during the full-scale tests, the jet pipe was found to set up a vibration in the rear of the fuselage and it is possible that this combined with the rear fuselage flexibility, which does not exist on the model, to cause an overall aircraft pitch.

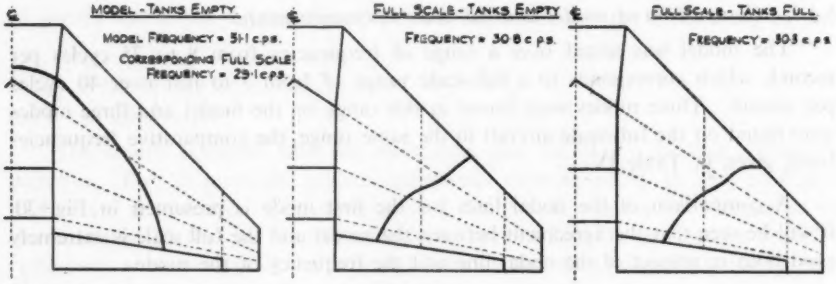
MODEL - TANKS EMPTY
MODEL FREQUENCY = 31·1 c.p.s.
CORRESPONDING FULL SCALE FREQUENCY = 29·1 c.p.s.
FULL SCALE - TANKS EMPTY
FREQUENCY = 30·8 c.p.s.
FULL SCALE - TANKS FULL
FREQUENCY = 30·3 c.p.s.

Fig. 31.
Resonant mode comparison.

TABLE IV

Resonance Frequencies (cycles/second).

	Model frequency (tanks empty)	*Predicted for full scale (tanks empty)*	*Observed full scale (tanks empty)*	*Observed full scale (tanks full)*
1st Mode	33.4	19.0	19.1	18.8
2nd Mode	51.1	29.1	30.8	30.3
3rd Mode	67.4	38.2	39.9	39.2

For the third mode, the frequency agreement is again good but the nodal line comparison is poor. At a mode as high as the third, it is possible that the discrepancy is largely due to the differences in the mounting of the aircraft and the model, and the position of the undercarriage, since the full-scale aircraft stood on its tyres whereas the model was mounted about its centre of gravity with the undercarriage retracted, the latter being more representative of flight conditions. This is partly borne out by the fact that there is a large variation between the modes for tanks empty and tanks full; for the full-scale aircraft, although the fuel weight is 115 per cent. of the unladen wing weight, whereas the undercarriage is only 30 per cent., the undercarriage is mounted farther outboard than the fuel and is more concentrated. It is hoped that further research will be done to determine the effect of undercarriage position.

To summarise, it would appear that the Xylonite model has predicted the fundamental mode and frequency with great accuracy, but the higher modes have only been predicted as regards frequency, although differences in the higher modes may be due to differences in the method of mounting.

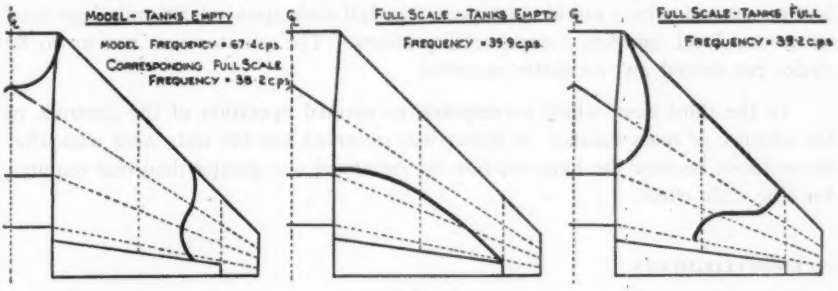
MODEL - TANKS EMPTY
MODEL FREQUENCY = 67·4 c.p.s.
CORRESPONDING FULL SCALE FREQUENCY = 38·2 c.p.s.
FULL SCALE - TANKS EMPTY
FREQUENCY = 39·9 c.p.s.
FULL SCALE - TANKS FULL
FREQUENCY = 39·2 c.p.s.

Fig. 32.
Resonant mode comparison.

7. The Flutter Tests

The flutter tests were done in a wind tunnel at the Royal Aircraft Establishment, and for these tests the tunnel mounting to be used was as described for the resonance tests, and as shown in Fig. 25. In addition to this mounting, it was necessary to fit a grab, so that in the event of flutter occurring while the model was under test in the tunnel the grab could be brought into action and so prevent damage, or possible loss, of the model. This grab is shown in the "off" position on Fig. 25. Also for tunnel tests, a small electric motor with out-of-balance masses on the ends of its shaft was built into the model fuselage to excite flutter vibrations.

It has been shown in Section 2.4 that

$$V_{cF}/V_{cM} = \{ E_{DF}\gamma_M/(E_{DM}\gamma_F) \}^{\frac{1}{2}}$$

and since $E_{DF} = 10 \times 10^6$ lb./in.^{2}

$$E_{DM} = 0.51 \times 10^6 \text{ lb./in.}^2$$

$$\gamma_F = 0.103 \text{ lb./in.}^3$$

$$\gamma_M = 0.049 \text{ lb./in.}^3$$

$$V_{cF}/V_{cM} = \{ (10/0.51) \times (0.049/0.103) \}^{\frac{1}{2}} = 3.06.$$

Hence the full-scale critical speed would be 3.06 times the model critical speed.

The model was tested in three conditions:—

(*i*) Elevons locked.

(*ii*) Elevons free with full mass balance.

(*iii*) Elevons free with no mass balance.

In the first two cases tests were done up to the maximum tunnel speed of 286 feet per second, which would correspond to a full scale speed of 596 miles per hour at ground level, ignoring compressibility effects. The vibrator was run up to 80 cycles per second and no flutter occurred.

In the third case, which corresponds to manual operation of the controls, in the absence of mass balance no flutter was observed but the tests were somewhat inconclusive because the hinge friction on the model was greater than that required for true scale effect.

ACKNOWLEDGMENTS

The scheme of research described in this paper was undertaken by Boulton Paul Aircraft Ltd. as a result of a Ministry of Supply contract, and the authors

wish to acknowledge the encouragement given by the Ministry throughout the work and to thank them, and Boulton Paul Aircraft Ltd., for permission to publish this work.

Thanks are also due to H. H. Dixon for the preparation of the drawings and the design of the test rigs, and to E. N. Armstrong, who constructed the model.

REFERENCES

1. REDSHAW, S. C. and ARTHUR, R. E. (1943). A Method of Investigating the Stiffness of a Structure by Means of a Xylonite Model. A.R.C. Report 7432, 1943.

2. BAKER, D. A. (1944). The Effect of Atmospheric Humidity on the Strength and Dimensions of Thermo-Plastics. Report No. Mat.N./2/3007, 1944.

3. LAWTON, T. S., CARSWELL, T. S. and NASON, H. K. (1945). Effect of Some Environment Conditions on the Mechanical Properties of Cellulose Acetate and Cellulose Nitrate Plastic Sheets. *Transactions of the A.S.M.E.*, Vol. 67, No. 1, 1945.

4. BRUHN, E. F. (1945). Tests on Thin-Walled Celluloid Cylinders to Determine the Interaction Curves under Combined Bending, Torsion and Compression or Tension Loads. N.A.C.A. Tech. Note 951, 1945.

5. PINOIR, R. and DUBOIS, A. (1948). Mesure du Module d'Young des Fils et Films par une Methode Dynamique. *Le Journal de Physique et le Radium*, Série VIII, Tome IX, 1948.

6. CORNU, A. (1869). *Comptes Rendus*, Vol. 69, p. 333, 1869.

7. SEARLE, G. F. C. (1933). *Experimental Elasticity*, Cambridge University Press, 1933.

8. REDSHAW, S. C. (1944). A Note on the Use of Models for Aeroplane Flutter Analysis. A.R.C. Report 7653, 1944.

9. FRAZER, R. A. and DUNCAN, W. J. (1928). The Flutter of Aeroplane Wings. R. & M. No. 1155, 1928.

10. SCRUTON, C. and LAMBOURNE, N. C. (1944). Note on the Proposed Use of Xylonite for the Construction of Models for Flutter Investigations. A.R.C. Report 7673, 1944.

11. HOWARTH, R. M. (1945). Stress-strain Diagrams. M.A.P. Scientific and Technical Memoranda No. 14/45, 1945.

A Note on the Stressing of Oleo-Pneumatic Shock Absorbers

D. M. A. LEGGETT, M.A., Ph.D., A.F.R.Ae.S.
(*Reader in Applied Mathematics, King's College, University of London*)

Summary: This note investigates the stresses set up in the hollow circular cylinders which form part of most oleo-pneumatic shock absorbers. The cylinders are subject to combined axial loading and internal pressure, and one, at least, of the ends is built in. Although the size of cylinder and type of loading are representative of the shock absorbers in certain types of tail wheel unit, the investigation also applies to various designs of hydraulic jack.

It is shown that the maximum stress which occurs is usually due to the prevention of circumferential expansion at a built-in end, and that the maximum bending stress thus induced is approximately $\sqrt{3}$ times the corresponding hoop stress. Although in practice the maximum stress in the cylinder will often be less than the maximum theoretical stress because of local yielding of the material, this very yielding is a source of weakness which may easily give rise to failure by fatigue. There is little doubt that directly or indirectly these high bending stresses have, on occasion, been the cause of failure.

1. Introduction

In general an oleo-pneumatic shock absorber performs its function of transforming kinetic energy into potential and heat energy by means of a piston shown

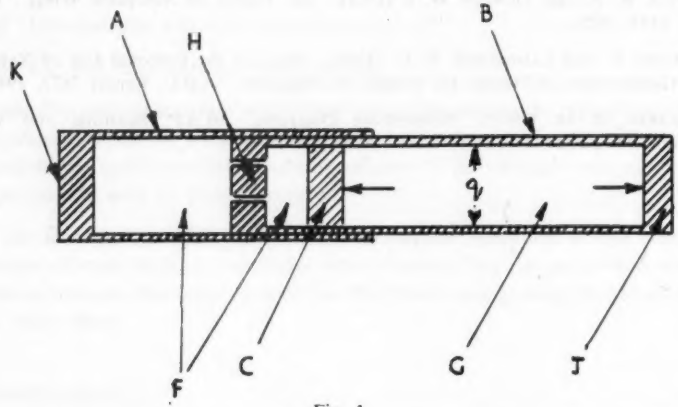

Fig. 1.

Paper received May 1951.
[The Aeronautical Quarterly, Vol. III, September 1951]

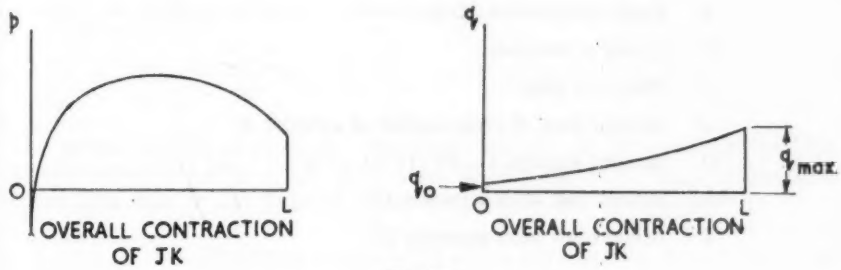

Fig. 2.*

diagrammatically in Fig. 1. The piston consists of two circular cylinders A and B free to slide in one another, and a floating plunger C. The spaces F and G contain oil and compressed air respectively, and the end H of the cylinder B contains small orifices through which oil can be forced under pressure. As soon as a load is applied, the ends J and K are forced together and energy is absorbed by compressing the air in G and by forcing oil through the orifices in H.

Denoting the air pressure in G by q, and the compressive axial stress in the walls of the cylinder B by p, the variation of p and q during the operation of the shock absorber is illustrated graphically in Fig. 2.

When a hollow cylinder, *e.g.* B in Fig. 1, is subjected to a combination of axial loading and internal pressure such as that shown in Fig. 2, an excessive hoop stress is usually regarded as the most likely cause of failure. Tests, however, have indicated that this explanation is inadequate, since on a number of occasions the wall of the cylinder B has failed by bulging outwards near the built-in end J for a value of the hoop stress appreciably below the yield stress of the material.

The object of this note is to investigate the cause of this type of failure so that it can be guarded against in future design.

Notation

t	thickness of cylinder wall
r	mean of internal and external radii of cylinder
w	radial displacement of point in middle surface of cylinder
q	internal pressure
q_o, q_{max}	initial and maximum values of q

*Denoting the internal area of cross section of the cylinder B by α, purely statical considerations show that the values of p at the beginning and end of the stroke (when the applied load is a maximum, the air and oil pressures are equal, and the whole system is momentarily at rest) are $-q_o \alpha/(2\pi rt)$ and q_{max} respectively.

p axial compressive stress

E Young's modulus

ν Poisson's ratio

α internal area of cross section of cylinder B

D flexural rigidity, *i.e.* $Et^3/[12(1-\nu^2)]$

θ, ϕ defined just after equation (3)

ψ defined just after equation (5)

2. Statement of the Problem and its Theoretical Solution

The problem considered is the behaviour of a hollow circular cylinder under combinations of axial loading and internal pressure of the type shown in Fig. 2. It is assumed that the cylinder is uniform, that the end J is built in, and that the maximum stress in the cylinder does not exceed the elastic limit of the material of which it is made.

The functioning of the shock absorber induces the following three distinct sets of stresses in the cylinder wall:—

(*a*) a uniform axial stress p,

(*b*) hoop stresses due to internal pressure q,

(*c*) bending stresses due to prevention of circumferential expansion at the built-in end J.

Of these, the axial stress p is given by Fig. 2, and the hoop stress is qr/t, but evaluation of the bending stresses requires analysis.

2.1. *Mathematical analysis*

Timoshenko[1] has shown that the radial displacement of the middle surface of a hollow circular cylinder due to a combination of axial loading and internal pressure must satisfy the differential equation

$$D\frac{d^4w}{dx^4} + pt\frac{d^2w}{dx^2} + \frac{Etw}{r^2} = q + \frac{\nu pt}{r} \quad . \quad . \quad . \quad (1)$$

A particular integral of this equation is

$$[r^2/(Et)]\,(q + \nu pt/r) \quad . \quad . \quad . \quad . \quad . \quad (2)$$

and the complementary function is

$$\{ A\cos\phi x + B\sin\phi x \}\, e^{\theta x} + \{ L\cos\phi x + M\sin\phi x \}\, e^{-\theta x} \quad . \quad (3)$$

where A, B, L, M are arbitrary constants, and θ and ϕ are given by

$$\theta = \left\{ -\frac{pt}{4D} + \tfrac{1}{2}\left(\frac{Et}{r^2 D}\right)^{\frac{1}{2}} \right\}^{\frac{1}{2}}, \quad \phi = \left\{ \frac{pt}{4D} + \tfrac{1}{2}\left(\frac{Et}{r^2 D}\right)^{\frac{1}{2}} \right\}^{\frac{1}{2}}.$$

The general solution of (1) is the sum of (2) and (3), and it remains to find the arbitrary constants A, B, L, M. Since a solution in which w increases without limit is not applicable, A and B are zero and the general solution reduces to

$$w = [r^2/(Et)]\,(q + \nu pt/r) + \{ L\cos\phi x + M\sin\phi x \}\, e^{-\theta x}. \qquad (4)$$

Apart from the constant term, it follows that for all positive θ, w dies away exponentially except for the special case in which θ is zero; w is then entirely periodic and the cylinder buckles throughout its length into circumferential waves. The value of the compressive stress for which this happens is $Et/[r\{3(1-\nu^2)\}^{\frac{1}{2}}]$, in agreement with the classical value obtained by more rigorous methods, but is not of any practical interest here since, for the kind of cylinder being considered, it is greatly in excess of the compressive yield stress of the material.

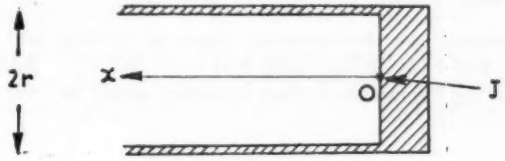

Fig. 3.

The remaining constants L and M are found from the fact that the cylinder is built in at the end J, so that when x is zero, w and dw/dx both vanish. Substituting the values thus obtained for L and M in (4),

$$w = [r^2/(Et)]\,(q + \nu pt/r)\,\{ 1 - e^{-\theta x}\,\mathrm{cosec}\,\psi \sin(\phi x + \psi) \} \qquad (5)$$

where $\psi = \sin^{-1}[\phi/(\theta^2+\phi^2)^{\frac{1}{2}}]$.

It is now possible to evaluate the local bending stresses near the built-in end J. For given x, the maximum bending stress is $\pm(Et/2)(d^2w/dx^2)$, *i.e.* using (5),

$$\pm\tfrac{1}{2}r^2\,(q + \nu pt/r)\,[(\theta^2+\phi^2)^{\frac{1}{2}}/\phi]\, e^{-\theta x}\sin(\psi - \phi x). \qquad (6)$$

Since (6) is greatest in absolute magnitude when x is zero, the value of the maximum bending stress is

$$(r/t)(q + \nu pt/r)\,\{3(1-\nu^2)\}^{\frac{1}{2}} \qquad (7)$$

In practice the rate of increase of q exceeds the rate of decline of $\nu pt/r$; hence the bending stress given by (7) is a maximum when q is a maximum, having the value

$$(r/t)\,q_{\max}\,\{\,3\,(1-\nu^2)\,\}^{\frac{1}{4}}.$$

It will be noted that this expression is approximately $\sqrt{3}$ times the value of the corresponding hoop stress.

3. Example Typical of the Shock Absorbers in a Tail Wheel Unit

Mean radius of cylinder (r)	0.85 in.
Thickness of cylinder wall (t)	0.06 in.
Young's modulus (E)	30×10^6 lb./in.^{2}
Poisson's ratio (ν)	0.25
Yield stress of material	6.0×10^4 lb./in.^{2}
Maximum value of internal pressure ($q_{\max}$)	3.5×10^3 lb./in.^{2}
Maximum value of axial compressive stress (p)	3.0×10^4 lb./in.^{2}

For this particular case the maximum values of the hoop and bending stresses are respectively 4.95×10^4 lb./in.^{2} and 8.31×10^4 lb./in.^{2}. Buckling could not possibly occur, as the compressive stress necessary would be over 10^6 lb./in.^{2}

4. Conclusion

For a cylinder typical of those used in most oleo-pneumatic shock absorbers, the maximum stress which occurs is usually due to the prevention of circumferential expansion at a built-in end; the maximum bending stress so induced is $\sqrt{3}$ times the corresponding hoop stress. Although in practice the maximum stress will often be less than the maximum theoretical stress because of local yielding of the material, this very yielding is a source of weakness which may easily lead to fatigue failure. For cylinders representative of those used in the shock absorbers of certain tail wheel units, there is little doubt that these very high bending stresses have, on occasion, been the cause of failure.

Reference

1. Timoshenko, S. (1936). *Theory of Elastic Stability*, Chap. 9, McGraw-Hill, 1936.

The Flow of an Incompressible Fluid through an Axial Turbo-Machine with any Number of Rows

J. W. RAILLY, M.Sc., A.M.I.Mech.E.
(Department of Mechanical Engineering, The University, Birmingham)

Summary: A method is described whereby, at any point in an infinite parallel annulus, the approximate axial velocity due to a single row of high aspect ratio blades may be calculated from a knowledge of the conditions of flow adjacent to the blades. The method is based on the assumption of a simplified expression for the radial velocity, being the product of an unknown function of the radius and an exponential term independent of the radius containing an undetermined constant; the function and the undetermined constant are calculated by reference to the conditions of flow in the plane of the row considered. The flow due to any number of rows is then obtained by summing the radial velocity fields due to each row and obtaining the axial velocities by integration of the equation of continuity.

The solution of the problem with infinitely many rows is shown to have a simple form by virtue of the fact that the flow (provided that the velocities remain finite) settles down to a pattern which is periodic by one stage pitch.

1. Introduction

The problem of the flow of a perfect, incompressible fluid in a multi-stage axial turbo-machine is beyond exact mathematical treatment except in one or two special cases where the flow is a potential flow, as in the well-known "free vortex" flow with radial blades or, in the special case treated by Traupel[1], of curved stator blades in infinite array. For rotational flow the equations are no longer linear and approximate methods must be adopted to obtain a solution.

The well-known method based on the assumption of radial equilibrium between the rows is liable to yield misleading results due to the neglect of the axial derivative of the radial velocity, which becomes very important between the normally closely-pitched rows of multi-stage compressors and turbines.

This effect was taken into account by Traupel[1], who assumed that in an axially-symmetric multi-stage machine with an infinite number of identical stages, the stream function, being periodic by one stage pitch, could be represented by the first term of a Fourier series so that an expression could be obtained for the radial

Paper received November 1950.
[The Aeronautical Quarterly, Vol. III, September 1951]

velocity. A solution of the equations in radial planes situated midway between the rows was then possible.

A brilliant treatment of the problem along the lines of classical aerofoil theory has been made by Marble[2], who derived a linear equation for the radial velocity on either side of a discontinuity (by which the blade row was replaced). The solution for the arbitrary blade row of finite axial width then follows by superposition. The method is difficult to use when more than one row is to be considered because of the continual approximation that is necessary to take account of the equivalent of the Kutta-Joukowski condition at the trailing edge of the blades, namely, that the flow angle there must always have the given variation with the radius.

The method developed in this paper uses one of the results of Traupel and Marble's work, namely, that the radial velocity is of the form (for an isolated row at the axial co-ordinate $z=(i-1)\beta$)

$$u=\sum_{p=1}^{\infty} e^{\pm k_p\{z-(i-1)\beta\}} f(k_p r) \text{ for } z \lesseqgtr (i-1)\beta.$$

Accordingly a simple form for the radial velocity distribution is assumed as follows

$$u=e^{\pm k_i\{z-(i-1)\beta\}} f_i(r) \quad . \quad . \quad . \quad . \quad . \quad (1)$$

where k_i is an undetermined constant and $f_i(r)$ an unknown function.

Notation

C_1, C_2	constants of integration
p	an integer
E	mechanical energy of flow, per unit mass
f_i	radial velocity function of i^{th} row
k_i	radial velocity "attenuation" constant for i^{th} row
K_i	function of k_i
r	radius
R	outer radius
u, v, w	radial, peripheral and axial components of velocity
$\overline{w}$	mean axial velocity
W	energy increment in rotor element per unit mass
z	co-ordinate parallel to axis
α_1, α_2	rotor inlet and outlet angles

α_3, α_4	stator inlet and outlet angles
w_0	axial velocity at infinity upstream
β	axial pitch of rows
ξ, η, ζ	vorticity components, radial, peripheral and axial
ϕ, ψ	functions of the radius and axial velocity at a row
Ω	angular velocity of rotor
$'$	conditions before a row
$''$	conditions after a row

SUFFIXES

i, s	number of row
n	number of rows
m	mean value
R	rotor
C	stator

2. Theory

2.1. *Single isolated row*

The theory is developed first for a single row. Starting from the equation of continuity in axially-symmetric flow (cylindrical polar co-ordinates)

$$\partial u/\partial r + u/r + \partial w/\partial z = 0 \qquad (2)$$

whence
$$w(z) - w(-\infty) = -\int_{-\infty}^{z} \left(\frac{\partial u}{\partial r} + \frac{u}{r}\right) dz$$

i.e.,
$$w(z) - w(-\infty) = -\left(f_i'(r) + \frac{f_i(r)}{r}\right) \frac{1}{k_i} \left[e^{k_i\{z-(i-1)\beta\}}\right]_{-\infty}^{z}$$

Thus
$$w(\overline{i-1}\,\beta) - w(-\infty) = -\frac{1}{k_i}\left[f_i'(r) + \frac{1}{r} f_i(r)\right]. \qquad (3)$$

Similarly,
$$w(\infty) - w(\overline{i-1}\,\beta) = -\frac{1}{k_i}\left[f_i'(r) + \frac{1}{r} f_i(r)\right], \qquad (4)$$

and subtracting

$$w(\infty) + w(-\infty) = 2\, w(\overline{i-1}\,\beta) \qquad (5)$$

i.e. the axial velocity at the row is midway between the velocity far upstream and far downstream—a well-known result. At any point z then

$$z<(i-1)\beta, \quad w(z)-w(-\infty)=[w(\infty)-w(\overline{i-1}\,\beta)]\,e^{k_i\{z-(i-1)\beta\}}$$

$$z>(i-1)\beta, \quad w(z)-w(-\infty)=[w(\infty)-w(\overline{i-1}\,\beta)]\,(2-e^{-k_i\{z-(i-1)\beta\}})$$

Or these may be written

$$w(z)-w(\overline{i-1}\,\beta)=\phi_i K_i\{z-(i-1)\beta\} \quad . \quad . \quad . \quad . \quad (6)$$

where $K_i(z)=1-e^{-k_i z}, \quad z>0, \quad K(-z)=-K(z)$

and $$\phi_i=w(\infty)-w(\overline{i-1}\,\beta) \quad . \quad . \quad . \quad . \quad . \quad (7)$$

If k_i is known, then the axial velocity distribution is given in terms of $w(\overline{i-1}\,\beta)$, at the row, and ϕ_i.

Referring now to the first equation of motion in cylindrical polar co-ordinates (for axi-symmetric flow) which is, in the absence of radial forces

$$v\zeta-w\eta=\partial E/\partial r \quad . \quad . \quad . \quad . \quad . \quad (8)$$

and then writing $$\zeta=\frac{1}{r}\frac{\partial}{\partial r}(vr), \quad \eta=\frac{\partial u}{\partial z}-\frac{\partial w}{\partial r},$$

the equation $$\frac{v}{r}\frac{\partial}{\partial r}(vr)-w\left(\frac{\partial u}{\partial z}-\frac{\partial w}{\partial r}\right)=\frac{\partial E}{\partial r} \quad . \quad . \quad . \quad . \quad (8a)$$

is obtained.

Considering a single row of blades at $z=(i-1)\beta$ we have approximately, ignoring the actual radial slope and displacement of the stream lines (-0 and $+0$ indicating positions immediately upstream and downstream of the row)

$$\left(\frac{\partial E}{\partial r}\right)_{z=-\infty}\simeq\left(\frac{\partial E}{\partial r}\right)_{z=-0}, \quad \left(\frac{\partial E}{\partial r}\right)_{z=+\infty}\simeq\left(\frac{\partial E}{\partial r}\right)_{z=+0},$$

while $$v(-\infty)\simeq v(-0)=v'$$

$$v(+\infty)\simeq v(+0)=v''$$

at any radius. Writing equation (8*a*) for both sides of the row and subtracting

$$w(\overline{i-1}\,\beta)\left\{\left(\frac{\partial u}{\partial z}\right)_{+0}-\left(\frac{\partial u}{\partial z}\right)_{-0}\right\}=\frac{v''}{r}\frac{d}{dr}(v''r)-\frac{v'}{r}\frac{d}{dr}(v'r)-\frac{d}{dr}(E''-E')$$

noticing that the axial velocity, $w(\overline{i-1}\,\beta)$ is continuous across the discontinuity. If W is the increment of mechanical energy (if any) at the row then

$$\frac{d}{dr}(E''-E')=\frac{dW}{dr}.$$

Writing $\psi_i(r)=\frac{1}{2}\left\{\left(\frac{\partial u}{\partial z}\right)_{+0}-\left(\frac{\partial u}{\partial z}\right)_{-0}\right\}$, we have

$$\psi_i(r)=\frac{1}{2\,w(\overline{i-1}\,\beta)}\left[\frac{v''}{r}\frac{d}{dr}(v''r)-\frac{v'}{r}\frac{d}{dr}(v'r)-\frac{dW}{dr}\right] \quad . \quad . \quad (9)$$

Referring again to the radial velocity expression, equation (1), then

$$\left(\frac{\partial u}{\partial z}\right)_{+0}=-k_i f_i(r)=-\left(\frac{\partial u}{\partial z}\right)_{-0}$$

whence $$\psi_i(r)=-k_i f_i(r) \quad . \quad . \quad . \quad . \quad . \quad . \quad (10)$$

Obtaining ϕ_i in terms of $f_i(r)$ from equations (7) and (4), then

$$-r\phi_i k_i=\frac{d}{dr}\{r f_i(r)\}$$

which yields on integration, assuming k_i constant

$$r f_i(r)-f_i(1)=-k_i\int_1^r r\phi_i\,dr \quad . \quad . \quad . \quad . \quad . \quad (11)$$

Now $f_i(1)$ must be zero, since the radial velocity at the walls must be zero. This implies that $\psi(1)$, by equation (10), must also be zero, a result that will not follow from equation (9). This contradiction arises because of the amount of approximation in neglecting much of the influence of the radial velocity; only a "mean" value may be obtained for the constant k_i for the row. Eliminating $f_i(r)$ between equations (10) and (11)

$$k_i^2=r\psi_i(r)\Big/\int_1^r r\phi_i(r)\,dr.$$

Integrating both numerator and denominator between the limits of 1 and R the value of k_i for row "i" is obtained as

$$k_i^2=\int_1^R r\psi_i(r)\,dr\Big/\int_1^R\int_1^r r\phi_i(r)\,dr^2 \quad . \quad . \quad . \quad (12)$$

Far upstream and downstream of the row, the term $\partial u/\partial z$ in equation (8*a*) must disappear (*i.e.* radial equilibrium is established). Hence

$$\frac{1}{2}\frac{d}{dr}\{w^2(-\infty)\} + \frac{v'}{r}\frac{d}{dr}(rv') = \frac{dE(-\infty)}{dr}$$

$$\frac{1}{2}\frac{d}{dr}\{w^2(+\infty)\} + \frac{v''}{r}\frac{d}{dr}(rv'') = \frac{dE(+\infty)}{dr}.$$

Subtracting and using equation (5)

$$2\frac{d}{dr}\left[[w(\infty) - w(\overline{i-1}\,\beta)]\, w(\overline{i-1}\,\beta)\right] = \frac{dW}{dr} - \frac{v''}{r}\frac{d}{dr}(v''r) + \frac{v'}{r}\frac{d}{dr}(v'r)$$

whence $$2\phi_i w(\overline{i-1}\,\beta) = W - \int \frac{v''}{r}\frac{d}{dr}(v''r)\,dr + \int \frac{v'}{r}\frac{d}{dr}(v'r)\,dr + \text{constant} \quad . \quad (13)$$

The constant is determined from the condition that $\int_1^R r\phi\,dr$ must be zero

Thus, given the axial velocity $w(\overline{i-1}\,\beta)$ at the row at the point $z=(i-1)\beta$, a complete solution is obtained of the problem of the single isolated row. The whirl velocity is assumed to be known upstream of the row and the whirl velocity downstream follows from the known outlet angle of the row.

2.2. *Solution with more than one row*

The problem of more than one row is considered on the basis of the solution for a single row. That this is possible follows from the fact that the velocity field surrounding a single row may be determined from the knowledge of the velocities in the plane of the row. Indeed, no advantage follows for the solution for the single row in this form due to the fact that the velocity profile upstream cannot be assumed at the outset.

Replacing each of the rows by a discontinuity as before, it is clear that if the variation of radial velocity throughout the machine is given, the axial velocities must follow by integration of the equation of continuity, given the axial velocity at one plane (usually the velocity at infinity upstream). The assumption is now made that the radial velocity field in the multi-stage machine is the sum of each of the radial velocity fields due to each of the rows acting individually, provided that the axial velocities and whirl velocities remain the same for the row in each case. Initially, neither axial nor radial velocities will be known in the plane of each of the rows, but an initial assumption is made for the axial velocities, the corresponding radial velocity fields are calculated and they are added together. Then the axial velocities may be re-calculated and by this process of successive approximation the

solution* is obtained. The whirl velocities in each case will be calculated afresh from the velocity triangles. For a series of n rows, separated by an equal length β, the expression for the resultant radial velocity $u(z)$ is obtained; thus

$$u(z)=\sum_{i=1}^{n} u_i(z)=\sum_{i=1}^{n} f_i(r)\, e^{\pm k_i\{z-(i-1)\beta\}} \quad . \quad . \quad . \quad (14)$$

$$\text{with} \begin{cases} +\text{sign for } z<(i-1)\beta \\ -\text{sign for } z>(i-1)\beta . \end{cases}$$

Hence if w_0 is the velocity at infinity upstream of all rows (assumed to be uniform in this instance) then

$$w(z)-w_0=-\int_{-\infty}^{z}\sum_{1}^{n} e^{\pm k_i\{z-(i-1)\beta\}}\left(\frac{f_i(r)}{r}+f'(r)\right)dz$$

$$=\sum_{1}^{n}\int_{-\infty}^{z} k_i\,\phi_i\, e^{\pm k_i\{z-(i-1)\beta\}}dz$$

changing the order of summation and using equation (11). This becomes

$$w(z)-w_0=\sum_{1}^{n}\phi_i\left(\left[e^{+k_i\{z-(i-1)\beta\}}\right]_{-\infty}^{(i-1)\beta}+\left[e^{-k_i\{z-(i-1)\beta\}}\right]_{(i-1)\beta}^{z}\right),\quad z>(i-1)\beta$$

$$\text{or}\quad \sum_{1}^{n}\phi_i\left(\left[e^{+k_i\{z-(i-1)\beta\}}\right]_{-\infty}^{z}\right) \qquad z<(i-1)\beta$$

Inserting the limits

$$w(z)-w_0=\sum_{1}^{n}\phi_i\left(2-e^{-k_i\{z-(i-1)\beta\}}\right)\ \text{or}\ \sum_{1}^{n}\phi_i\, e^{k_i\{z-(i-1)\beta\}}.$$

Putting $z=(s-1)\beta$ for the velocity at the s^{th} row,

$$w\overline{(s-1}\,\beta)-w_0=\sum_{1}^{s}\phi_i\left(2-e^{-k_i\{(s-1)\beta\}}\right)+\sum_{s+1}^{n}\phi_i\, e^{k_i\{(s-1)\beta\}} \quad . \quad . \quad . \quad . \quad (15)$$

Thus, for a machine with four rows, four explicit relations are obtained for

*In the evaluation of the ψ-functions for each row the radial velocities due to adjacent rows do not enter, as the only discontinuity in $\partial u/\partial z$ is that of the radial velocity associated with the row in question.

the axial velocities in the plane of the rows by writing $s=1, 2, 3, 4$ in equation (15),

$$
\begin{aligned}
w_1 - w_0 &= \phi_1 && + \phi_2 e^{-k_2\beta} && + \phi_3 e^{-2k_3\beta} && + \phi_4 e^{-3k_4\beta} \\
w_2 - w_0 &= \phi_1 (2 - e^{-k_1\beta}) && + \phi_2 && + \phi_3 e^{-k_3\beta} && + \phi_4 e^{-2k_4\beta} \\
w_3 - w_0 &= \phi_1 (2 - e^{-2k_1\beta}) && + \phi_2 (2 - e^{-k_2\beta}) && + \phi_3 && + \phi_4 e^{-k_4\beta} \\
w_4 - w_0 &= \phi_1 (2 - e^{-3k_1\beta}) && + \phi_2 (2 - e^{-2k_2\beta}) && + \phi_3 (2 - e^{-k_3\beta}) && + \phi_4 .
\end{aligned}
$$

For only two rows we have

$$
\left.
\begin{aligned}
w_1 - w_0 &= \phi_1 + \phi_2 e^{-k_2\beta} \\
w_2 - w_0 &= \phi_2 + \phi_1 (2 - e^{-k_1\beta})
\end{aligned}
\right\} \quad . \quad . \quad . \quad . \quad (15a)
$$

As β approaches zero, the axial velocity becomes common to the two rows.

2.3. *Solution with infinitely many rows. "Ultimate steady flow"*

The "ultimate steady flow" is the state that prevails when there are infinitely many identical stages and the flow pattern repeats itself (as was shown by Howell[3]) with a periodicity of one stage pitch. Thus at every rotor or stator row the conditions are identical.

In some special cases this flow cannot be established, due to the fact that infinite velocities and infinite throughput are required. Hence, specifying finite velocities throughout

$$w_R\,,\ \phi_R = \text{constant for all rotor rows}$$

$$w_C\,,\ \phi_C = \text{constant for all stator rows,}$$

w and ϕ having their previous meanings. The radial velocity at any point z is given by

$$
u = \sum_{-\infty}^{s} e^{-k_i(z-(i-1)\beta)} f_i(r) + \sum_{s+1}^{\infty} e^{k_i(z-i\beta)} f_i(r) \quad . \quad . \quad . \quad (16)
$$

where $(s-1)\beta \leqslant z \leqslant s\beta$.

Substituting into equation (3) and integrating between the limits of $z=(s-1)\beta$ and $z=s\beta$, then

$$
w(s\beta) - w(\overline{s-1}\,\beta) = \sum_{-\infty}^{s} \phi_i (1 - e^{-k_i\beta}) e^{-k_i\{(s-i)\beta\}} + \sum_{s+1}^{\infty} \phi_i (1 - e^{-k_i\beta}) e^{-k_i\{(s-i)\beta\}}.
$$

Assigning to ϕ_i the values ϕ_R, ϕ_C, ϕ_R, and so on, as $i=s$, $s+1$, $s+2$ and $i=s$, $s-1$, $s-2$, and so forth, we obtain

$$w(s\beta)-w(\overline{s-1}\,\beta)= \phi_R(1-e^{-k_R\beta})(1+e^{-k_R\beta}+e^{-2k_R\beta}+\ \ldots$$
$$+\phi_C(1-e^{-k_C\beta})(1+e^{-k_C\beta}+e^{-2k_C\beta}+\ \ldots$$

Thus, taking the sums to infinity

$$w_{s+1}-w_s = \phi_R+\phi_C$$

$$w_{s+2}-w_{s+1}= \phi_R+\phi_C$$

and adding $$w_{s+2}-w_s =2(\phi_R+\phi_C)=0$$

whence $$w_{s+1}=w_s \text{ or } w_R=w_C.$$

That is, the axial velocity at the rotor rows is the same as that at the stator rows. The solution to the problem then follows rapidly from the condition that

$$dW/dr=0$$

over the rotor row. In between the rows the change in the axial velocity profile will depend on the row spacing, β, and may be calculated by integrating equation (16) between the limits $(s-1)\beta$ and z.

This solution should be compared with Traupel's solution for an infinite number of rows. In that case the solution was obtained with reference to a radial plane situated midway between the rows so that an alternating "shift" of flow is observed. It is to be expected that the present solution for the velocities will give values midway between those of Traupel.

A general rule to be observed, therefore, in the design of many stage axial-flow turbo-machines employing arbitrary blade loading with high aspect ratio, closely-pitched blades, is

(*a*) the axial velocity is the same in the plane of rotor and stator

(*b*) the work done is independent of the radius. Thus for any machine in which the rotor and stator outlet angles are a chosen function of radius we may write

$$W=\Omega r\{\Omega r-w(\tan\alpha_2+\tan\alpha_4)\}$$

giving $$w=\left(\Omega r-\frac{W}{\Omega r}\right)\frac{1}{\tan\alpha_2+\tan\alpha_4} \quad . \quad . \quad . \quad . \quad (17)$$

and W is obtained by integration as a function of the mean axial velocity, $\overline{w}$. Thus

$$\overline{w} = \frac{2}{R^2 - 1} \int_1^R \left(\Omega r^2 - \frac{W}{\Omega} \right) \left(\frac{1}{\tan \alpha_2 + \tan \alpha_4} \right) dr \quad . \quad . \quad . \quad (18$$

The blade inlet angles follow from the velocity triangles.

3. Example

The simple case is treated first of a single compressor stage upstream of which the swirl is zero, so that only two rows need be considered. The interesting case of blades which are untwisted is considered. In addition it is assumed for the stage that

$$\alpha_4 = 0; \quad (\tan \alpha_1 - \tan \alpha_2)_m = 0.66$$

$$\text{(mean blade speed)/(mean axial velocity)} = 1.40$$

$$\text{whence} \quad \alpha_2 = \tan^{-1} 0.74$$

$$\text{degree of reaction} = 76.5 \text{ per cent.}$$

Taking the hub radius as unity, the angular velocity of the rotor, Ω, becomes, with a radius ratio of 1.5

$$\Omega = \frac{\Omega r_m}{\overline{w}\,(r_m/r)} = 1.12 .$$

The first approximation to the axial velocity will be taken as the mean value, $\overline{w}$, which in this case is unity. ϕ is evaluated from equation (13), thus:—

For the rotor row "1":

$$2\phi_1 w_1 = \Omega r (\Omega r - w_1 \tan \alpha_2) - \int_1^r \frac{\Omega r - w_1 \tan \alpha_1}{r} \frac{d}{dr} (\Omega r^2 - r w_1 \tan \alpha_2)\, dr + C_1$$

For the stator row "2":

$$2\phi_2 w_2 = \int_1^r \frac{\Omega r - w_1 \tan \alpha_2}{r} \frac{d}{dr} (\Omega r^2 - r w_1 \tan \alpha_2)\, dr + C_2 \quad \text{with} \quad w_1 = w_2 = \overline{w} .$$

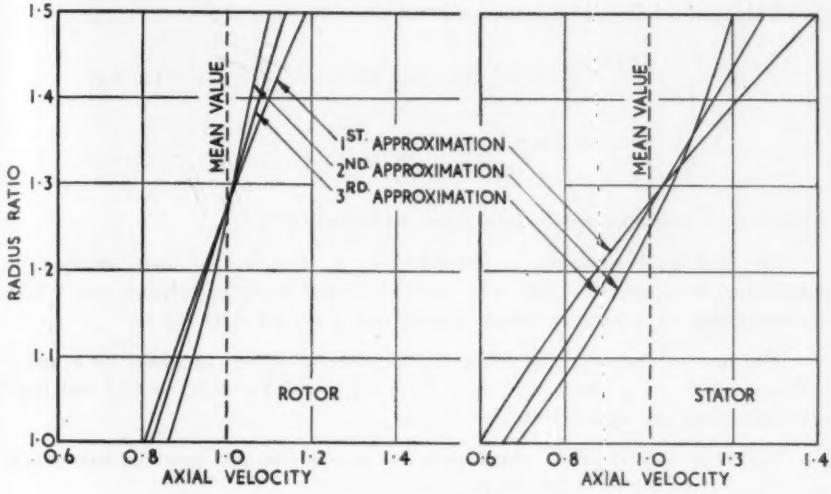

(a) SINGLE STAGE (2 ROWS)

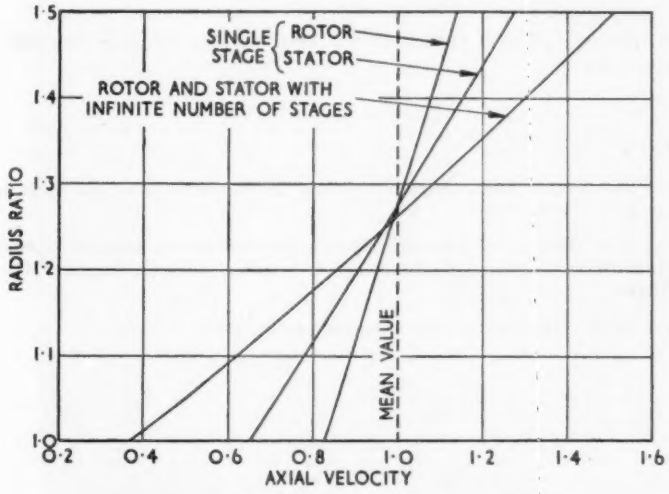

(b) SINGLE STAGE COMPARED WITH COMPRESSOR WITH INFINITELY MANY ROWS

Fig. 1.

Axial velocity profiles for (*a*) single stage and (*b*) infinite number of stages of untwisted compressor blading.

Values of ψ follow from equation (9):—

$$\psi_1 = \frac{1}{2w_1}\left[\frac{\Omega r - w_1 \tan \alpha_2}{r}\frac{d}{dr}(\Omega r^2 - rw_1 \tan \alpha_2) - \frac{d}{dr}(\Omega^2 r^2 - \Omega r \tan \alpha_2)\right]$$

$$\psi_2 = \frac{1}{2w_2}\left[\frac{\Omega r - w_1 \tan \alpha_2}{r}\frac{d}{dr}(\Omega r^2 - rw_1 \tan \alpha_2)\right]$$

whence k_1, k_2 are obtained by integration (equation (12)).

The first approximations to the velocities w_1 and w_2 are then obtained by substitution in equations (15*a*). The value of β used in the calculation was 1/5.25 corresponding to a ratio of (blade height/row pitch) of 2.63.

The new values of w_1, w_2 found then replace $\overline{w}$ in the equations for ϕ and ψ and new values of ϕ and k are found for each row. The first, second and third approximations are shown plotted in Fig. 1.

The flow with infinitely many rows is readily obtained from equations (17) and (18). Thus for $\overline{w}=1$, $W=0.95$.

Hence $$w = 1.513\,r - 1.145/r\,.$$

This relation is shown plotted to the same axes as the axial velocities for the single-stage case.

References

1. Traupel, W. (1942). Neue allgemeine Theorie der mehrstufigen axialen Turbomaschinen. Leeman & Co., Zurich, 1942.
2. Marble, F. E. (1948). The Flow of a Perfect Fluid through an Axial Turbo-machine with Prescribed Blade Loading. *Journal of the Aeronautical Sciences*, August 1948. Vol. 15, pp. 473-485.
3. Howell, A. R. (1942). R.A.E. Report (unpublished), 1942.

The Anti-Symmetric Vibrations of Aircraft

R. W. TRAILL-NASH, Ph.D.

(Department of Supply and Development, Aeronautical Research Laboratories, Melbourne)

Summary: It is assumed that pure anti-symmetric vibrations of an aircraft can exist, involving fuselage torsion but excluding fuselage bending. With this assumption, which in most cases is a reasonable approximation, the eigenvalue equations for anti-symmetric vibrations of a complete aircraft are derived in a very general form. The "lumped mass" approximation to the continuous mass distribution is used and sub-matrices are associated with properties of relatively simple branches of the system. The final eigenvalue equations are expressed in terms of these sub-matrices so that in a numerical application the physical system as such is considered only in relation to properties of the simple branches. It is assumed initially that the aircraft wing and tail have flexural axes of the conventional type, but the treatment is generalised to cover swept and cranked wing aircraft.

1. Introduction

In this paper a similar procedure to that of Ref. 1 is used to set up the eigenvalue equations for anti-symmetric vibrations of a complete aircraft.

General considerations relating to the representation of the system and the validity of calculated vibration characteristics are discussed in Ref. 1 and, as these are of equal relevance to anti-symmetric vibrations, reference should be made to the previous publication in reading the present paper. Although it has not been possible, in the interest of continuity, to avoid repetition of some material covered previously, an effort has been made to condense the treatment as far as is practicable; and where this is done a more detailed consideration of the point in question (or a similar one) is given under the corresponding section number of Ref. 1.

The eigenvalue equations for anti-symmetric vibrations of a conventional aircraft are derived in matrix notation[2] and are presented in a form which admits the adoption of any arbitrary number of degrees of freedom within the general geometric shape of the system. The "lumped mass" approximation to the continuous mass distribution is used and matrices are associated with relatively simple branches of the system. The derived equations are stated in terms of these matrices so that in an application to a particular aircraft the physical system as such

Paper received June 1950.

[The Aeronautical Quarterly, Vol. III, September 1951]

is considered only in relation to the properties of these simple branches. A purely formal process of numerical matrix multiplication and addition then yields the required eigenvalue equations.

The representation of the system is similar to that used by J. Morris and D. Morrison[3] but allows for torsional freedom of the wings and includes flexible tailplanes. In particular aircraft the effect of these additional types of freedom may be negligible, in which case they can be omitted; but certainly in large multi-engine aircraft wing torsion is important, and tailplane flexibility probably warrants consideration. In general the number of degrees of freedom in the representation will be limited by the computational facilities available, and the accuracy of frequencies and modes is then dependent on the choice of freedoms and associated inertias.

The assumption is made in the analysis that no fuselage bending takes place during vibration; this assumption implies that the fuselage flexural axis is straight and that there is symmetry about this axis. The existence of a tail fin (or tail fins) is the most obvious violation of this assumption, while it is also clear that in general the wing structure fails to satisfy this requirement. The limitation imposed on the system then takes the form of a constraint which suppresses fuselage bending, and as such it is to be expected that there should be a tendency for calculated natural frequencies to be higher than the corresponding experimental values. However, since the wings play the dominant role in the vibrations concerned it is reasonable to expect the lower order natural frequencies to show satisfactory agreement with experiment and the modal shapes of the wings to be not seriously in error.

2. Representation of Aircraft

In the idealised representation the continuous mass distribution is replaced by a finite number of masses, some of which, depending on the type of motion to which they are subjected during vibration, have associated moments of inertia. The representation of wings and tail planes is identical with that of Ref. 1 since the type of motion experienced by these branches is essentially the same in symmetric and anti-symmetric vibrations. On the fuselage the type of motion is different since here pure rotation (in the torsional sense) is assumed, while for symmetric vibrations the motion is in pure linear displacement. The fuselage is therefore represented by a finite number of polar moments of inertia (the magnitude and location of which are calculated to approximate to the continuous distribution) on a massless member of the prescribed torsional stiffness. In single fin aircraft, at the fuselage-tail junction the polar moment of inertia about the fuselage longitudinal axis is calculated to include the tail fin, which is assumed rigid. Strictly, similar moments of inertia should be associated with tail fins of dual fin aircraft, but it is doubtful if this refinement and consequent increase in complexity of the problem and labour of computation is justified in view of the already very approximate tail representation.

Because of the geometric symmetry assumption it is sufficient to consider only one half of the system lying to one side of the vertical plane of symmetry. When this is done it is understood that all inertias and stiffnesses on the fuselage refer to one half of the corresponding values for the complete system. As in Ref. 1 the elastic properties of the system are described by influence coefficients.

Figure 1 depicts a typical idealisation of a four-engine aircraft for analysis of anti-symmetric vibration modes. A flexural axis is initially assumed to exist in the wing and tail but this is not essential to the treatment and a generalisation to include swept and cranked wings is made in the Appendix.

3. Notation and Co-ordinates

As in Ref. 1 the system is free-free and therefore requires a datum within the system as a reference for elastic displacements. This point is selected at the fuselage-wing junction and elastic displacements are then measured relative to the tangent plane at the wing root. The subscript "fw" is associated with fuselage properties forward of the reference station, while "ft" is associated with fuselage properties aft of this point. The subscripts "w" and "t" are associated with wing and tail properties respectively.

Section 3.1

In accordance with this subdivision of the system the following notation for inertia properties is adopted*:

$(m_i)_w$	mass at i^{th} wing station
$(p_i)_w$	moment of inertia at i^{th} wing station
$(j_i)_{fw}$	moment of inertia at i^{th} station of fuselage forward of reference station
j_o	moment of inertia at reference station
$(j_i)_{ft}$	moment of inertia at i^{th} station of fuselage aft of reference station
$(m_i)_t$	mass at i^{th} tail station
$(p_i)_t$	moment of inertia at i^{th} tail station.

Section 3.2

The system is referred to Cartesian co-ordinates, the x co-ordinate measured parallel to the fuselage axis and positive in the tail-to-nose sense, the z-axis downwards; the y-axis completes a right-hand system. In the undistorted condition

*Moments of inertia on the fuselage are of the type relevant to inertia torques on the fuselage. Those on the wing and tail are of the type relevant to inertia torques on the wing and tail respectively.

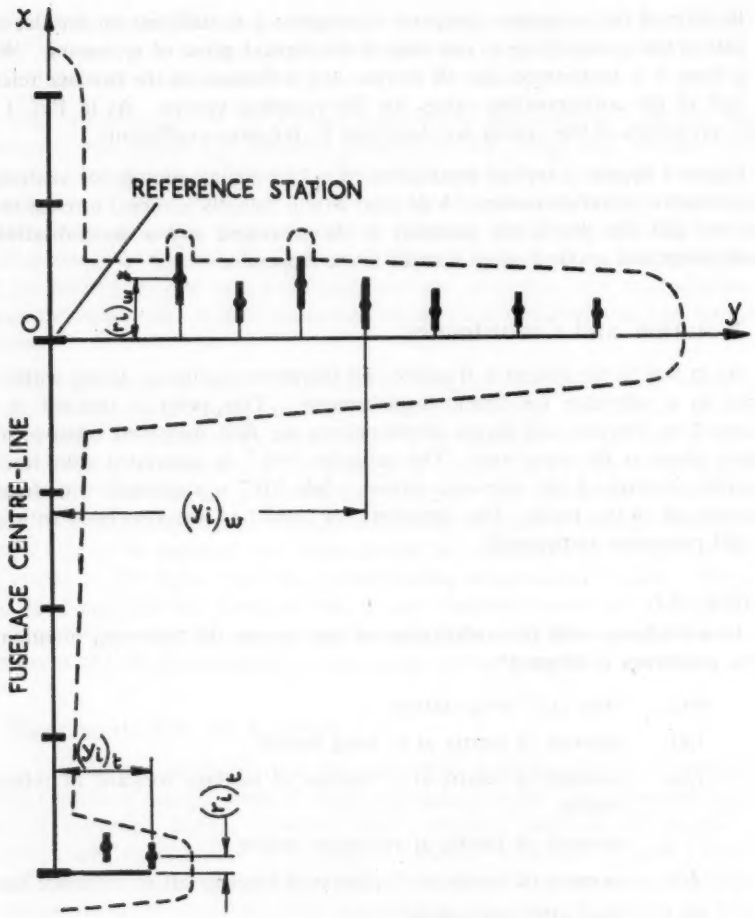

Fig. 1.
Idealised representation of aircraft.

the aircraft representation (assumed coplanar) is positioned to lie in the xy plane with the reference station at the origin.

Further constants relating to the geometry of the system are then defined as follows

$(r_i)_w$ distance of mass at i^{th} wing station from wing flexural axis

$(r_i)_t$ distance of mass at i^{th} tail station from tail flexural axis
(in both cases measured positive in the positive x direction)

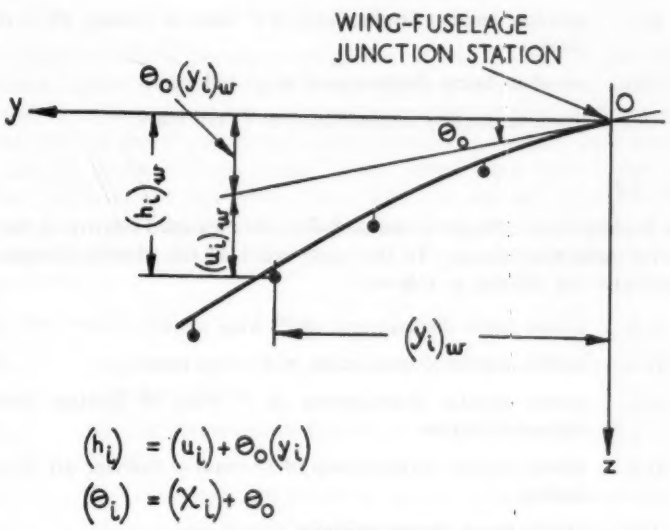

Fig. 2.
Displacement co-ordinates.

$(y_i)_w$ distance of mass at i^{th} wing station from fuselage axis

$(y_i)_t$ distance of mass at i^{th} tail station from fuselage axis.

Section 3.3

Displacements of the system initially appear in the equations of motion in two forms, one as absolute displacements which are associated with inertia forces and the other as relative displacements within the system which are associated with elastic forces. The absolute displacements are measured relative to the fixed co-ordinate axes and the notation is as follows* (*see* Fig. 2)

$(h_i)_w$ absolute linear displacement of i^{th} wing mass

$(\bar{\gamma}_i)_w$ absolute angular displacement of i^{th} wing mass

$(\theta_i)_{fw}$ absolute angular displacement of i^{th} mass of fuselage forward of reference station

θ_0 absolute angular displacement at reference station

*In accordance with the right-hand system of axes, linear displacements are measured positive downwards, pitching angular displacements positive in the nose up sense, and rolling angular displacements anti-clockwise looking aft. Angular displacements on the fuselage are of the fuselage torsion type, while those on the wing and tail are of the wing and tail torsion type respectively.

$(\theta_i)_{fa}$ absolute angular displacement of i^{th} mass of fuselage aft of reference station

$(h_i)_t$ absolute linear displacement at i^{th} tail mass

$(\varphi_i)_t$ absolute angular displacement at i^{th} tail mass.

Section 3.4

The displacements relevant to elastic forces are measured relative to the tangent plane at the reference station. In the same order as the absolute displacements, the co-ordinates are defined as follows*

$(u_i)_w$ elastic linear displacement of i^{th} wing mass

$(\psi_i)_w$ elastic angular displacement of i^{th} wing mass

$(\chi_i)_{fw}$ elastic angular displacement of i^{th} mass of fuselage forward of reference station

$(\chi_i)_{fa}$ elastic angular displacement of i^{th} mass of fuselage aft of reference station

$(u_i)_t$ elastic linear displacement of i^{th} tail mass

$(\psi_i)_t$ elastic angular displacement of i^{th} tail mass.

Section 3.5

The quantities so far defined refer to individual masses of the system and these are now grouped together in matrix form to give a more concise notation. When more than one matrix is associated with a particular branch of the system it is understood that the elements referring to specific stations occur in the same sequence in each matrix. The relevant matrices are defined in Table I.

The orders of these matrices depend on the representation of the system. In addition to those of the table certain "operational" matrices are defined as follows

I the unit matrix,

L a column matrix, each element of which is unity,

H a square matrix, each element of which is unity.

As in Ref. 1, the orders of these matrices are nowhere specially defined, and each may appear as matrices of different order in a single expression. The appropriate order of a particular operational matrix is implied by conditions of compatibility in the equation in which it occurs.

*Clearly the elastic angular displacements on the wing and tail are identical with the corresponding absolute angular displacements; but for the sake of uniformity, distinct symbols are introduced.

Section 3.6

It remains to define the elastic properties of the system. In the definitions which follow, square flexibility matrices are matrices of which the element in the i^{th} row and j^{th} column represents the displacement in the i^{th} co-ordinate produced by a unit force in the j^{th} co-ordinate under specified constraint conditions of the system. In this regard "displacement" and "force" may apply either to linear or angular displacement and either linear force or moment respectively. The conditions of constraint are: for the wing and tail, encastré conditions at the root; for the fuselage fore and aft of the reference station, encastré conditions at the reference station.

The matrices are defined as follows

Θ_{fw}^{-1} angular displacement flexibility matrix of fuselage forward of reference station

Θ_{ft}^{-1} angular displacement flexibility matrix of fuselage aft of reference station

E_w^{-1} linear displacement flexibility matrix on wing flexural axis

E_t^{-1} linear displacement flexibility matrix on tail flexural axis

Θ_w^{-1} angular displacement flexibility matrix of wing

TABLE I

Diagonal Matrix	*Elements*	*Column Matrix*	*Elements*
A_w	$(m_i)_w$	h_w	$(h_i)_w$
P_w	$(p_i)_w$	φ_w	$(\varphi_i)_w$
J_{fw}	$(j_i)_{fw}$	θ_{fw}	$(\theta_i)_{fw}$
J_{ft}	$(j_i)_{ft}$	θ_{ft}	$(\theta_i)_{ft}$
A_t	$(m_i)_t$	h_t	$(h_i)_t$
P_t	$(p_i)_t$	φ_t	$(\varphi_i)_t$
R_w	$(r_i)_w$	u_w	$(u_i)_w$
R_t	$(r_i)_t$	ψ_w	$(\psi_i)_w$
Y_w	$(y_i)_w$	χ_{fw}	$(\chi_i)_{fw}$
Y_t	$(y_i)_t$	χ_{ft}	$(\chi_i)_{ft}$
		u_t	$(u_i)_t$
		ψ_t	$(\psi_i)_t$

Θ_t^{-1}	angular displacement flexibility matrix of tail
g	column of angular displacements on fuselage aft of reference station due to unit moment (about fuselage axis) at fuselage-tail junction (a column of Θ_{ft}^{-1})
g'	(transposed of g) row of angular displacements at fuselage-tail junction due to unit moment (about fuselage axis) at fuselage mass stations aft of reference station (a row of Θ_{ft}^{-1})
η	angular displacement (about fuselage axis) at fuselage-tail junction due to a unit moment at this station (an element of Θ_{ft}^{-1}).

4. Inertia Forces

Forces acting in the undamped vibration of a free-free system are discussed briefly in Section 4 of Ref. 1. Inertia forces acting during vibration at a frequency of ω radians per second are

$$\text{linear force} = \omega^2 \times (\text{mass}) \times (\text{linear displacement})$$

$$\text{and moment} = \omega^2 \times (\text{moment of inertia}) \times (\text{angular displacement}).$$

The elastic displacements in the various branches of the system are now deduced in terms of these inertia forces. Again, as in Ref. 1 it is of advantage to consider in detail the inertia forces on the wing and tail. Fig. 3 depicts the conditions at a spanwise station of the wing. The linear inertia force at the i^{th} station is

$$(F_i)_w = \omega^2 (m_i)_w (h_i)_w \quad . \quad . \quad . \quad . \quad . \quad . \quad (1)$$

and the moment about the flexural axis is

$$(M_i)_w = \omega^2 \{ (p_i)_w (\varphi_i)_w - (r_i)_w (m_i)_w (h_i)_w \}, \quad . \quad . \quad (2)$$

where F is measured positive in the positive z direction (downwards) and M is measured positive anti-clockwise.

Similar expressions hold for forces at the i^{th} station of the tail. At the fuselage-tail junction the moment about the fuselage axis applied from the tail is given by

$$T = \omega^2 \sum_i (y_i)_t (m_i)_t (h_i)_t \quad . \quad . \quad . \quad . \quad (3)$$

or

$$T = \omega^2 L' Y_t A_t h_t \quad . \quad . \quad . \quad . \quad . \quad (4)$$

from Table I, where L' is the transposed of L.

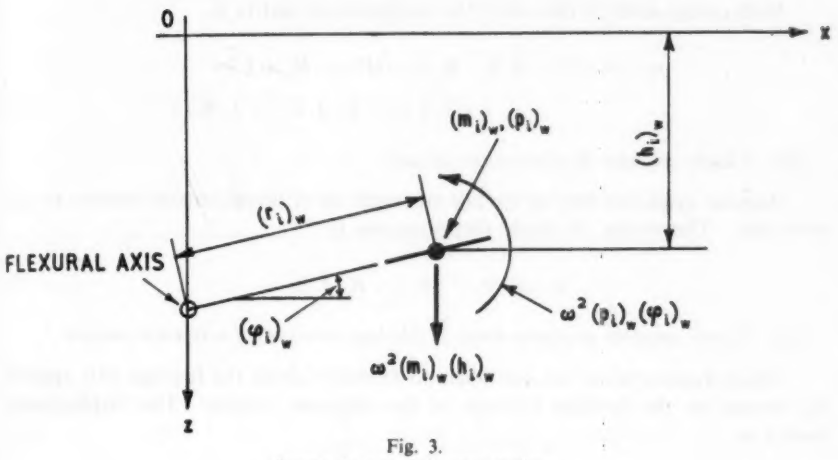

Fig. 3.
Inertia forces at i^{th} wing station.

5. Elastic Displacements

The elastic displacements in the various branches of the system are as follows:—

(*i*) *Elastic angular displacements of fuselage aft of reference station*

The elastic displacements consist of

(*a*) displacements due to moments from fuselage inertias,

(*b*) displacements due to moment from tail applied at fuselage-tail junction.

The displacement matrix with components in this order becomes

$$\chi_{ft} = \omega^2 \{ \Theta_{ft}^{-1} J_{ft} \theta_{ft} + g L' Y_t A_t h_t \} \quad . \quad . \quad . \quad (5)$$

(*ii*) *Elastic linear displacements of tail*

Elastic linear displacements on the tail depend on the displacements relative to the root, and the elastic displacement of the fuselage-tail junction. The components of displacement are

(*a*) tail flexural axis displacements at spanwise mass stations relative to tail root,

(*b*) displacements of masses relative to root due to torsion about flexural axis,

(*c*) displacements due to angular displacement of fuselage-tail junction about fuselage axis.

With components in this order the displacement matrix is

$$u_t = \omega^2 \{ E_t^{-1} A_t h_t - R_t \Theta_t^{-1} (P_t \varphi_t - R_t A_t h_t) + \\ + Y_t L (\eta L' Y_t A_t h_t + g' J_{ft} \theta_{ft}) \} \quad . \quad (6)$$

(*iii*) *Elastic angular displacements of tail*

Angular displacements on the tail are made up of displacements relative to the root only. The matrix of elastic displacements is

$$\psi_t = \omega^2 \Theta_t^{-1} \{ P_t \varphi_t - R_t A_t h_t \} \quad . \quad . \quad . \quad . \quad (7)$$

(*iv*) *Elastic angular displacements of fuselage forward of reference station*

These displacements are due solely to moments about the fuselage axis applied by inertias on the fuselage forward of the reference station. The displacement matrix is

$$\chi_{fw} = \omega^2 \Theta_{fw}^{-1} J_{fw} \theta_{fw} \quad . \quad . \quad . \quad . \quad (8)$$

(*v*) *Elastic linear displacements of wing*

These are of the same form as the displacements relative to the root on the tail. The components are

(*a*) wing flexural axis displacements

(*b*) displacements due to torsion about flexural axis.

The displacement matrix is

$$u_w = \omega^2 \{ E_w^{-1} A_w h_w - R_w \Theta_w^{-1} (P_w \varphi_w - R_w A_w h_w) \} \quad . \quad (9)$$

(*vi*) *Elastic angular displacements of wing*

Wing angular displacements are measured relative to the root and are given by

$$\psi_w = \omega^2 \Theta_w^{-1} \{ P_w \varphi_w - R_w A_w h_w \} \quad . \quad . \quad . \quad (10)$$

The equations (5)-(10) may be expressed more concisely in one matrix equation and it is easily verified that they are equivalent to (11), in which broken lines indicate partitioning into sub-matrices.

6. Equilibrium Conditions and Transformation of Co-ordinates

In order to express (11) in terms of one set of displacement co-ordinates the relation between the absolute displacements and the elastic displacements is now

$$
\begin{bmatrix} \chi_{ft} \\ \chi_{fw} \\ u_t \\ u_w \\ \psi_t \\ \psi_w \end{bmatrix} = \omega^2 \begin{bmatrix} \Theta_{ft}^{-1} & 0 & gL'Y_t & 0 & 0 & 0 \\ 0 & \Theta_{fw}^{-1} & 0 & 0 & 0 & 0 \\ Y_t Lg' & 0 & E_t^{-1} + R_t \Theta_t^{-1} R_t + \\ & & + \eta Y_t H Y_t & 0 & -R_t \Theta_t^{-1} & 0 \\ 0 & 0 & 0 & E_w^{-1} + R_w \Theta_w^{-1} R_w & 0 & -R_w \Theta_w^{-1} \\ 0 & 0 & -\Theta_t^{-1} R_t & 0 & \Theta_t^{-1} & 0 \\ 0 & 0 & 0 & -\Theta_w^{-1} R_w & 0 & \Theta_w^{-1} \end{bmatrix} \begin{bmatrix} J_{ft} & & & & & \\ & J_{fw} & & & & \\ & & A_t & & & \\ & & & A_w & & \\ & & & & P_t & \\ & & & & & P_w \end{bmatrix} \begin{bmatrix} \theta_{ft} \\ \theta_{fw} \\ h_t \\ h_w \\ \varphi_t \\ \varphi_w \end{bmatrix}
$$

Equation (11)

established. The component displacements on the wing are illustrated in Fig. 2 and it follows that

$$(h_i)_w = (u_i)_w + \theta_0 (y_i)_w \quad . \quad . \quad . \quad . \quad (12)$$

on the wing; also that a similar expression holds for the tail when the subscript "w" is replaced by "t." Also, on the fuselage,

$$(\theta_i) = (\chi_i) + \theta_0 \quad . \quad . \quad . \quad . \quad . \quad (13)$$

for subscripts "fw" and "ft."

The complete set of relations (12) and (13) may be expressed as

$$\begin{bmatrix} \theta_0 \\ \theta_{ft} \\ \theta_{fw} \\ h_t \\ h_w \\ \varphi_t \\ \varphi_w \end{bmatrix} = \begin{bmatrix} 0 \\ \chi_{ft} \\ \chi_{fw} \\ u_t \\ u_w \\ \psi_t \\ \psi_w \end{bmatrix} + \theta_0 \begin{bmatrix} 1 & & & & & & \\ & I & & & & & \\ & & I & & & & \\ & & & Y_t & & & \\ & & & & Y_w & & \\ & & & & & 0 & \\ & & & & & & 0 \end{bmatrix} \begin{bmatrix} 1 \\ L \\ L \\ L \\ L \\ L \\ L \end{bmatrix} \quad . \quad . \quad . \quad (14)$$

Let

$$\begin{bmatrix} h_t \\ h_w \end{bmatrix} = h, \begin{bmatrix} u_t \\ u_w \end{bmatrix} = u, \begin{bmatrix} \varphi_t \\ \varphi_w \end{bmatrix} = \varphi, \begin{bmatrix} \psi_t \\ \psi_w \end{bmatrix} = \psi, \begin{bmatrix} \theta_{ft} \\ \theta_{fw} \end{bmatrix} = \theta, \begin{bmatrix} \chi_{ft} \\ \chi_{fw} \end{bmatrix} = \chi,$$

$$\begin{bmatrix} Y_t & \\ & Y_w \end{bmatrix} = Y, \begin{bmatrix} A_t & \\ & A_w \end{bmatrix} = A, \begin{bmatrix} P_t & \\ & P_w \end{bmatrix} = P, \begin{bmatrix} J_{ft} & \\ & J_{fw} \end{bmatrix} = J \quad . \quad . \quad (15)$$

whence from (15), (14) becomes

$$\begin{bmatrix} \theta_0 \\ \theta \\ h \\ \varphi \end{bmatrix} = \begin{bmatrix} 0 \\ \chi \\ u \\ \psi \end{bmatrix} + \theta_0 \begin{bmatrix} 1 & & & \\ & I & & \\ & & Y & \\ & & & 0 \end{bmatrix} \begin{bmatrix} 1 \\ L \\ L \\ L \end{bmatrix} \quad . \quad . \quad . \quad (16)$$

Section 6.1

For equilibrium the sum of moments about the fuselage axis is zero. This condition may be written as

$$[1 \; L' \; L' \; L'] \begin{bmatrix} 1 & & & \\ & I & & \\ & & Y & \\ & & & 0 \end{bmatrix} \begin{bmatrix} j_0 & & & \\ & J & & \\ & & A & \\ & & & P \end{bmatrix} \begin{bmatrix} \theta_0 \\ \theta \\ h \\ \varphi \end{bmatrix} = 0, \quad . \quad . \quad (17$$

and substitution from (16) in (17) yields

$$[1\ L'\ L'\ L'] \begin{bmatrix} 1 & & \\ & I & \\ & Y & 0 \end{bmatrix} \begin{bmatrix} j_0 & & \\ & J & \\ & A & P \end{bmatrix} \begin{bmatrix} 0 \\ \chi \\ u \\ \psi \end{bmatrix} +$$

$$+\theta_0 [1\ L'\ L'\ L'] \begin{bmatrix} 1 & & \\ & I & \\ & Y & 0 \end{bmatrix} \begin{bmatrix} j_0 & & \\ & J & \\ & A & P \end{bmatrix} \begin{bmatrix} 1 & & \\ & I & \\ & Y & 0 \end{bmatrix} \begin{bmatrix} 1 \\ L \\ L \\ L \end{bmatrix} = 0 \quad . \quad (18)$$

$$\text{or}^* \quad \{ j_0 + L'JL + L'YAYL \} \theta_0 = -[L'\ L'\ L'] \begin{bmatrix} I & & \\ & Y & \\ & 0 & \end{bmatrix} \begin{bmatrix} J & & \\ & A & \\ & & P \end{bmatrix} \begin{bmatrix} \chi \\ u \\ \psi \end{bmatrix} \quad (19)$$

Thus θ_0 is defined in terms of the elastic displacements.

If $$\xi = \{ j_0 + L'JL + L'YAYL \}^{-1}, \quad . \quad . \quad . \quad (20)$$

then $$\theta_0 = -\xi [L'\ L'\ L'] \begin{bmatrix} I & & \\ & Y & \\ & 0 & \end{bmatrix} \begin{bmatrix} J & & \\ & A & \\ & & P \end{bmatrix} \begin{bmatrix} \chi \\ u \\ \psi \end{bmatrix} \quad . \quad . \quad . \quad (21)$$

Section 6.2

Substitution for θ_0 from (21) in (16) then yields

$$\begin{bmatrix} \theta \\ h \\ \varphi \end{bmatrix} = \left[\begin{bmatrix} I & & \\ & I & \\ & & I \end{bmatrix} - \xi \begin{bmatrix} I & & \\ & Y & \\ & 0 & \end{bmatrix} \begin{bmatrix} L \\ L \\ L \end{bmatrix} [L'\ L'\ L'] \begin{bmatrix} I & & \\ & Y & \\ & 0 & \end{bmatrix} \begin{bmatrix} J & & \\ & A & \\ & & P \end{bmatrix} \right] \begin{bmatrix} \chi \\ u \\ \psi \end{bmatrix}$$

$$. \quad . \quad . \quad . \quad . \quad . \quad . \quad (22)$$

where the square matrix on the right hand side is the matrix of co-ordinate transformation.

The equation (11) can now be expressed in terms of the elastic displacement co-ordinates alone, and substitution of (22) in (11) yields the required eigenvalue equations. The inertia matrix of (11) is post-multiplied by the matrix of co-ordinate transformation and the resulting product is the generalised inertia matrix corresponding to the elastic displacement co-ordinates.

---

*The coefficient of θ_0 is the moment of inertia of the system about the fuselage axis.

Let B denote this generalised inertia matrix. It is defined as

$$\begin{bmatrix} B \end{bmatrix} = \begin{bmatrix} J & A \\ & P \end{bmatrix} \times \text{the transformation matrix,}$$

or
$$\begin{bmatrix} B \end{bmatrix} = \begin{bmatrix} J & A \\ & P \end{bmatrix} - \zeta \begin{bmatrix} J & A \\ & 0 \end{bmatrix} \begin{bmatrix} I & Y \\ & 0 \end{bmatrix} \begin{bmatrix} H \end{bmatrix} \begin{bmatrix} I & Y \\ & 0 \end{bmatrix} \begin{bmatrix} J & A \\ & 0 \end{bmatrix} \quad . \quad (23)$$

The eigenvalue equations for anti-symmetric vibrations are then of the form

$$\begin{bmatrix} \chi \\ u \\ \psi \end{bmatrix} = \omega^2 \begin{bmatrix} D \end{bmatrix} \begin{bmatrix} B \end{bmatrix} \begin{bmatrix} \chi \\ u \\ \psi \end{bmatrix} \quad . \quad . \quad . \quad . \quad (24)$$

where D is the flexibility matrix in (11) and B is the generalised inertia matrix (23).

7. Summary of Analysis

The preceding analysis leads to a statement of the eigenvalue equations for anti-symmetric vibrations in a concise form. For numerical work on a particular aircraft it is necessary merely to insert the appropriate values of the physical properties in the final equations and the problem is set up for solution without explicit consideration of dynamics. In this section the results are summarised to provide all the necessary information for the calculation of the eigenvalue equations.

The equations are

$$\begin{bmatrix} \chi \\ u \\ \psi \end{bmatrix} = \omega^2 \begin{bmatrix} D \end{bmatrix} \begin{bmatrix} B \end{bmatrix} \begin{bmatrix} \chi \\ u \\ \psi \end{bmatrix} \quad . \quad . \quad . \quad . \quad (24)$$

where $\chi = \begin{bmatrix} \chi_{ft} \\ \chi_{fw} \end{bmatrix}$, $u = \begin{bmatrix} u_t \\ u_w \end{bmatrix}$, $\psi = \begin{bmatrix} \psi_t \\ \psi_w \end{bmatrix}$

and the elements with subscripts are defined in Table I and Section 3.4;

D is the flexible matrix (first square matrix on right hand side of (11));

B is the generalised inertia matrix (23), and in respect to (23),

$$J = \begin{bmatrix} J_{ft} \\ & J_{fw} \end{bmatrix}, \quad A = \begin{bmatrix} A_t \\ & A_w \end{bmatrix}, \quad P = \begin{bmatrix} P_t \\ & P_w \end{bmatrix}, \quad Y = \begin{bmatrix} Y_t \\ & Y_w \end{bmatrix}$$

and the elements with subscripts are defined in Table I and Sections 3.1 and 3.2,

I is the unit matrix,

H is a square matrix, each element of which is unity, and ζ is defined in (20).

Solution of (24) yields the natural frequencies and associated elastic displacements modes. The absolute displacement modes are then obtained from (14), Section 6, with the use of (21).

8. Solution of Equations

As in Ref. 1, once set up in numerical form the equations may be solved by any convenient method. It is suggested that matrix iteration[4] or the escalator method[5] is suitable.

APPENDIX

A discussion of flexural axis consideration is to be found in the Appendix of Ref. 1. The generalisation of the flexibility matrix D of (11) to cover the more general elastic properties is set out in Table II.

TABLE II

Location in D		*Modification*
Row	*Column*	
4	4	$(E_w^{-1} + R_w \Theta_w^{-1} R_w)$ is replaced by matrix whose elements a_{ij} denote linear displacement of i^{th} mass of wing due to unit linear force at j^{th} mass (root encastré)
4	6	$(-R_w \Theta_w^{-1})$ is replaced by matrix whose elements a_{ij} denote linear displacement of i^{th} mass of wing due to unit moment at j^{th} spanwise station (root encastré)
6	4	$(-\Theta_w^{-1} R_w)$ is replaced by matrix whose elements a_{ij} denote angular displacement at i^{th} spanwise wing station due to unit linear force at j^{th} mass (root encastré) (transposed of above)
6	6	Θ_w^{-1} is the matrix whose elements a_{ij} denote angular displacement at i^{th} wing station due to unit moment at j^{th} station (root encastré)

Similar modifications may be necessary for matrices relating to the tail. Table II applies similarly to the tail when the subscript "t" replaces "w," "tail" replaces "wing" and the row and column numbers are ordered as follows: 3,3; 3,5; 5,3; 5,5.

REFERENCES

1. TRAILL-NASH, R. W. (1951). The Symmetric Vibrations of Aircraft. *The Aeronautical Quarterly*, Vol. III, May 1951.

2. FRAZER, R. A., DUNCAN, W. J. and COLLAR, A. R. (1946). *Elementary Matrices*, Cambridge University Press, 1946.

3. MORRIS, J. and MORRISON, D. (1945). The Rolling Vibrations of an Aircraft, R.A.E. Report No. Vib. 8, August 1945.

4. DUNCAN, W. J. and COLLAR, A. R. (1934). A Method for the Solution of Oscillation Problems by Matrices. *Phil. Mag.* S7, Vol. 17, No. 115, May 1934, p. 865.

5. MORRIS, J. and HEAD, J. W. (1944). The "Escalator" Process for the Solution of Lagrangian Frequency Equations. *Phil. Mag.* S7, Vol. 35, No. 350, Nov., 1944, p. 735.